Response of Meridional Wind to Greenhouse Gas Forcing, Arctic Sea-Ice Loss, and Arctic Amplification

XIAODAN CHEN[a] AND AIGUO DAI[b]

[a] *Department of Atmospheric and Oceanic Sciences and Institute of Atmospheric Sciences, Fudan University, Shanghai, China*
[b] *Department of Atmospheric and Environmental Sciences, University at Albany, State University of New York, Albany, New York*

(Manuscript received 14 January 2022, in final form 17 July 2022)

ABSTRACT: Under increasing greenhouse gases, the Arctic warms about twice as fast as elsewhere, known as Arctic amplification (AA). AA weakens meridional temperature gradients and is hypothesized to weaken zonal wind and cause wavier circulation with stronger meridional wind (v) over northern mid-to-high latitudes. Here model simulations are analyzed to examine the v response to increased CO_2 and AA alone. Total v changes are found to be dominated by the effect of increased CO_2 without AA, with a zonal wavenumber-4 (wavenumber-3) change pattern over the northern (southern) extratropics that generally enhances current v and results partly from changes in zonal temperature gradients. The extratropical v change patterns are quasi-barotropic and are more pronounced during boreal winter. The CO_2 forcing also causes baroclinic v changes over the tropics tied to convection changes. The impact of AA on v is mainly over the northern extratropics and is opposite to the effect of increased CO_2 but with smaller magnitude. An eastward shift (~5° longitude) and an amplitude increase (~1 m s^{-1}) in the climatology of the northerlies over Europe caused mainly by CO_2 forcing contribute to the drying in southern Europe, while both AA and CO_2 forcing enhance the climatology of the northerlies over East Asia. Over the northern mid-to-high latitudes, Arctic sea ice loss and AA enhance the land–ocean thermal contrast in winter, while increased CO_2 alone weakens it, resulting in opposite changes in zonal temperature gradients and thus v. Different warming rates over land and ocean also contribute to the intermodel spread in v response patterns among climate models.

SIGNIFICANCE STATEMENT: Meridional wind (v) greatly contributes to thermal and moisture advection due to large meridional gradients in these fields. It is hypothesized that the enhanced Arctic warming under anthropogenic global warming could weaken meridional temperature gradients, decelerate westerly jets, and cause wavier circulation with stronger v over northern extratropics. Using novel climate model simulations, we found that the effect of increased CO_2 without AA determines the total v changes. AA generally weakens the climatological v, contrary to the direct effect of increased CO_2. The v changes are small relative to its climatology but may have large impacts on regional climate over central Europe, East Asia, and interior North America. More research is needed to examine the mechanisms causing regional v changes.

KEYWORDS: Arctic; Atmospheric circulation; Climate change; Climate models

1. Introduction

Due to large equator-to-pole gradients in air temperature and water vapor content, meridional wind (v) plays an important role in atmospheric thermal advection and moisture transport, thereby affecting temperature and precipitation variations and extremes over the midlatitudes (e.g., Shoji et al. 2014; Chen et al. 2021). Since the 1970s, the Arctic has been warming up more than twice as fast as the rest of the world (mainly in the boreal cold season) associated with a rapid decline in Arctic sea ice extent (Dai et al. 2019), a phenomenon known as Arctic amplification (AA) (Serreze and Francis 2006). Large AA (Arctic-to-global warming ratio > 1.4) is often associated with and likely caused by Arctic sea ice loss (Dai et al. 2019; Jenkins and Dai 2021). Coupled with oceanic processes, the atmospheric response to sea ice loss can extend to the tropics and even spread across the globe (Deser et al. 2015; England et al. 2020). Dai and Song (2020) showed that AA can weaken the meridional temperature gradient ($\partial T/\partial y$) over the northern mid-to-high latitudes, weakening the middle-upper tropospheric zonal wind (u). The weakened u is hypothesized to favor wavier midlatitude jets and amplified stationary waves, leading to stronger v wind and thus frequent cold surges and cold winters over the northern mid-to-high latitudes (Francis and Vavrus 2012, 2015; Liu et al. 2012).

This hypothesis has been supported by some observational studies that indicated larger and more persistent atmospheric Rossby waves in the northern mid-to-high latitudes as Arctic sea ice decreases in recent decades (e.g., Francis and Vavrus 2012, 2015; Luo et al. 2018; Xue et al. 2017), which favors cold surges and snowy winters in the northern midlatitudes (Liu et al. 2012), although the results are sensitive to seasons, metrics, and reanalysis datasets (Barnes 2013). The enhanced intraseasonal high-frequency waviness may accumulate over time to generate a seasonal-mean anomaly if it is spatially locked; for example, more frequent atmospheric blockings over the Ural Mountains can promote northerly winds from the Arctic into Eurasian midlatitudes, leading to overall colder winters there (e.g., Mori et al. 2014; Luo et al. 2016; Yao et al. 2017; Luo et al. 2019). Data for the last two

Corresponding authors: Aiguo Dai, adai@albany.edu; Xiaodan Chen, chenxd@fudan.edu.cn

DOI: 10.1175/JCLI-D-22-0023.1

decades, however, show a reversed waviness tendency despite the ongoing AA and Arctic sea ice loss (Blackport and Screen 2020), which suggests that the observed waviness changes are unlikely to be caused by long-term sea ice loss and AA, but may be due to other factors, such as internal multidecadal variability. Many modeling studies found that Arctic sea ice loss or reduced $\partial T/\partial y$ has little influence on midlatitude wave amplitudes (Hassanzadeh et al. 2014; Blackport and Screen 2020; Tierney et al. 2021). However, a wave power analysis showed enhanced power for eastward propagating large-scale ($\geq 10^4$ km) waves from 1950–2005 to 2006–99 in models from phase 5 of the Coupled Model Intercomparison Project (CMIP5), while smaller-scale waves will weaken (Sussman et al. 2020). Also, Arctic sea ice loss and the associated AA have been suggested to weaken the stratospheric polar vortex via upward-propagating waves, whose downward influence can in turn lead to weaker tropospheric westerly jets, stronger v, and more cold air outbreaks in the northern midlatitudes (Kim et al. 2014; Nakamura et al. 2016; Zhang et al. 2018; Chen et al. 2021; Cohen et al. 2021). However, the zonally asymmetric tropospheric response to the zonally symmetrical stratospheric anomalies has not been fully understood (e.g., Hitchcock and Simpson 2014). Nevertheless, an AA-induced strengthening in midlatitude v has been widely considered as a likely explanation for recent climate and weather extremes over the northern midlatitudes.

Considerable efforts have been made to understand the u response to increasing greenhouse gases (GHGs) and AA. Multiple reanalysis datasets show an increase in midlatitude u through the troposphere and a poleward shift of the tropospheric jet over both hemispheres in boreal winter since 1979 (Davis and Birner 2017; Manney and Hegglin 2018). One exception is that the midlatitude u over the North Atlantic decreased since 1979 from the surface to the 500-hPa level but increased from 500 hPa to the tropopause (Lee et al. 2019). Under increasing GHGs, the projected u change is characterized by a strengthening and a poleward shift of subtropical jets in both hemispheres, despite the low confidence over the Northern Hemisphere, especially over the North Atlantic due to the large internal variability and structural uncertainty in models (Lee et al. 2021). The poleward shift and acceleration of the midlatitude jets may result from increased $\partial T/\partial y$ in the middle to upper troposphere over the subtropics, the sloped tropopause, and increased transient eddies on the poleward flank of the jets (Lu et al. 2008). Large lower-tropospheric warming over the Arctic in response to Arctic sea ice loss is found in atmospheric models (Alexander et al. 2004; Deser et al. 2010), which weakens $\partial T/\partial y$ and baroclinicity over the northern mid-to-high latitudes that in turn reduces the midlatitude u and drives the midlatitude jets equatorward (Sun et al. 2015; Zhang et al. 2018; Peings et al. 2021). The u response to Arctic sea ice loss is amplified in coupled model simulations (Deser et al. 2015, 2016). Dai and Song (2020) compared the effect of AA alone to the effect of increased CO_2 without AA in climate model simulations and found that AA weakens u slightly only by ~10% in the middle to upper troposphere over 45°–75°N in response to a quadrupling of the preindustrial CO_2 ($4 \times CO_2$), while the effect of CO_2 increasing without AA is to strengthen tropospheric u by 10%–20% over 45°–85°N, leading to an overall strengthening in tropospheric u over these latitudes. However, given the relatively small GHG increase since the 1970s (compared to the $4 \times CO_2$ change), any recent u changes are likely due to natural climate fluctuations (including those in Arctic sea ice) rather than GHG-induced changes (Dai and Song 2020).

Compared with many studies on the u changes, there are relatively few studies on the v response to AA and increased GHGs, despite the fact that v plays an important role for regional temperature and precipitation variations. Haarsma and Selten (2012), Simpson et al. (2016), and Wills et al. (2019) showed that the multimodel mean v response to future warming near the end of the twenty-first century in CMIP3 and CMIP5 models is characterized as a zonal wavenumber-5 pattern around 30°N associated with a circumglobal waveguide in the subtropical upper troposphere during boreal winter, but there is a large intermodel spread (Simpson et al. 2016). Dai and Deng (2021) found a zonal wavenumber-4 pattern for tropospheric v changes over the Northern Hemispheric mid-to-high latitudes in response to $4 \times CO_2$. Other studies found significant regional v changes. For instance, the East Asian winter monsoon (EAWM), a strong northeasterly along the coasts of East Asia in boreal winter, undergoes a significant strengthening in reanalysis and observational datasets from 1990 to 2014 (Wang and Chen 2014) and in climate model projections under 2.0°C global warming (Miao et al. 2020). The northerly wind over central Europe in winter is projected to strengthen near the end of the twenty-first century in CMIP5 models (Tuel et al. 2021).

Potential mechanisms for the v changes have been examined. Based on the barotropic vorticity equation, Haarsma and Selten (2012) showed that the middle and upper tropospheric v change pattern over the Northern Hemisphere, which is strongest in the subtropics, can be largely explained by the Rossby wave response to tropical divergence changes associated with the weakening of the Walker circulation. They also showed that the effect of the strengthened zonal-mean u on the extratropical v change pattern is negligible compared to the zonally asymmetrical forcing (e.g., adiabatic heating and transients). However, using an idealized stationary wave model, Simpson et al. (2016) found that the upper-tropospheric v changes along the subtropical jets are caused mainly by the zonal-mean u acceleration in the subtropical upper troposphere via lengthening the dominant scale of the stationary waves with zonal wavenumbers ≥ 4. This mechanism may not work for the lower-tropospheric v changes because the circumglobal wave train–like changes around the subtropical jets is not evident in lower levels (Wills et al. 2019; Tuel et al. 2021). Besides stationary wave changes, differential warming rates over land and ocean may also contribute to the v change patterns (Dai and Deng 2021; Tuel and Eltahir 2020). Dai and Deng (2021) found a zonal wavenumber-4 v change pattern at 850 hPa over 40°–80°N in response to $4 \times CO_2$ that matches the change pattern in zonal temperature gradient ($\partial T/\partial x$), which is related to the land–ocean configuration. Tuel and Eltahir (2020) revealed comparable contributions from the regional land–ocean thermal contrast and upper-level stationary waves shift to the v changes around the Mediterranean Sea projected by CMIP5

models. Overall, the v response to increasing GHGs and the mechanisms involved are not well understood.

Most of the above analyses focused on the overall projected v changes in response to increased GHGs. Very few studies examined the v change in response to the Arctic sea ice loss and the associated AA. Dai and Song (2020) isolated the zonal-mean v change in response to AA from the total v response to global warming using coupled model simulations with 1% per year CO_2 increases with and without AA. They found that the effect of AA is largely masked by the opposite effect from increased CO_2 even in the boreal cold season when AA is strongest, suggesting that the effect of AA on zonal-mean v change is negligible. Dai and Deng (2021) examined the 850-hPa v change pattern north of 40°N in response to AA under $4 \times CO_2$ and found that AA generally exhibits an opposite effect compared with the effect from increased CO_2 without AA. While the previous studies have provided important information on how v might change under GHG-induced global warming, a comprehensive analysis of the v response to AA and the background warming without AA in the global troposphere is lacking, and whether Arctic sea ice loss and associated AA can strengthen midlatitude v is still unclear.

This study attempts to examine the long-term v response to the Arctic sea ice loss and associated AA, compare it to the effect from GHG forcing alone (without large AA; i.e., an Arctic-to-global warming ratio ≤ 1.4), analyze the effects on the current v climatology, and investigate the underlying mechanisms. Different from previous studies that focused on the overall v response near the end of the twenty-first century under a high emissions scenario (Haarsma and Selten 2012; Simpson et al. 2016; Wills et al. 2019), our study separates the v change pattern in response to increasing CO_2 into two components: with and without the effect of AA. Specifically, we want to address the following key questions: 1) How does v respond to GHG forcing (without large AA) and the Arctic sea ice loss (and associated AA) separately over the globe through the troposphere? 2) How do these v changes impact the climatological v pattern? Does AA enhance the current v pattern as hypothesized in previous studies? 3) Are these v responses related to the changes in atmospheric convection, zonal-mean zonal flow ($[u]$), and zonally asymmetric warming (e.g., $\partial \Delta T/\partial x$)?

Our main results are based on a set of coupled model simulations using the Community Earth System Model version 1.2.1 (CESM1) (Hurrell et al. 2013) with and without large AA and sea ice loss used previously by Dai et al. (2019), Dai and Song (2020), and Dai and Deng (2021). Historical and SSP5–8.5 simulations from 36 models in phase 6 of the Coupled Model Intercomparison Project (CMIP6) were used to access the overall forced v changes across different models. To validate the CESM1-simulated v response to AA, we further examined a pair of experiments based on three coupled models participating in the Polar Amplification Model Intercomparison Project (PAMIP; Smith et al. 2019).

Below we first describe the data, experiments, and methods in section 2. The v change patterns in response to AA and increased CO_2 alone and their impacts on v climatology are presented in section 3. Section 4 examines the potential causes of the extratropical v change patterns. Conclusions and discussion are given in section 5.

2. Model simulations and analysis method

a. Model simulations

We analyzed three CESM1 coupled simulations used in our previous studies (Dai et al. 2019; Dai and Song 2020; Dai and Deng 2021): a 150-yr preindustrial control run (CTL), a single 235-yr standard 1% CO_2 run (1%CO_2) with fully coupled sea ice dynamics and 1% per year CO_2 increase, and another single run (FixedIce) that is the same as the 1%CO_2 run but with fixed sea ice concentration (SIC) north of 30°N. Compared with the 1%CO_2 run, the only change in the FixedIce run is the use of daily SIC interpolated from the monthly climatology from the CTL run, instead of using the model internally calculated SIC as in the 1%CO_2 run, to estimate the sea ice and ocean-water fractions of the grid boxes north of 30°N that were used in the coupler module to calculate the gridbox mean values for all the ice–air, ice–ocean, and ocean–air exchange fluxes of mass, energy, and momentum. Sea ice was allowed to evolve dynamically inside the sea ice model in FixedIce, although the use of fixed SIC inside the coupler alters the surface fluxes, which leads to small sea ice loss and AA in the FixedIce run (Dai et al. 2019). Unlike many previous studies, this novel approach avoids adding ghost forcing (Deser et al. 2015, 2016; McCusker et al. 2017; Sun et al. 2018) or using unrealistic ice albedo (Blackport and Kushner 2017) to alter sea ice concentrations inside the sea ice model (Smith et al. 2017). More details on the FixedIce run can be found in Dai et al. (2019) and Dai and Song (2020).

These simulations were run with 2.5° longitude × ~2° latitude grids and 26 vertical levels from the surface to 3.5 hPa for the atmosphere and with ~1° grids for the ocean and sea ice models. The CESM1 is a fully coupled, comprehensive model of the Earth climate system that simulates the current climate fairly realistically (Hurrell et al. 2013). It has been widely used to study the Arctic, midlatitude, and global climate (Deser et al. 2015, 2016; Dai et al. 2019; Dai and Song 2020). The CESM1 CTL run simulates the time-mean v pattern and its variance seen in ERA5 reanalysis (Hersbach et al. 2020) reasonably well (figure not shown), with a global pattern correlation of 0.77 and 0.82 ($p < 0.01$ for both cases) for the mean v pattern at 850 and 300 hPa, respectively.

Following Dai and Song (2020), we used the changes in the 1%CO_2 and FixedIce runs relative to CTL climatology to represent, respectively, the overall response to CO_2-induced global warming (including the effect of AA) and the response to CO_2-induced background warming (without large AA and sea ice loss). Given that the Arctic sea ice loss and AA are greatly reduced in the FixedIce run (Dai et al. 2019; Dai and Song 2020), the difference between the 1%CO_2 and FixedIce runs largely represents the effect of AA and the occurring Arctic sea ice loss alone without the effect of the background warming.

TABLE 1. Summary of the CESM1, CMIP6, and PAMIP simulations analyzed in this study.

Simulations	Model name/names	Key references	Aim
CTL, 1% CO_2, FixedIce	CESM1	Dai et al. 2019; Dai and Song 2020	For separating the effect of AA and the effect of increased CO_2 without AA
CMIP6 historical (1970–99) and SSP5–8.5 (2070–99) simulations	36 models: ACCESS-CM2, ACCESS-ESM1-5, AWI-CM-1-1-MR, BCC-CSM2-MR, CAMS-CSM1-0, CanESM5, CAS-ESM2-0, CESM2, CESM2-WACCM, CIESM, CMCC-CM2-SR5, CMCC-ESM2, E3SM-1-1, EC-Earth3, EC-Earth3-CC, EC-Earth3-Veg, EC-Earth3-Veg-LR, FGOALS-f3-L, FGOALS-g3, FIO-ESM-2-0, GFDL-CM4, GFDL-ESM4, IITM-ESM, INM-CM4-8, INM-CM5-0, IPSL-CM6A-LR, KACE-1-0-G, KIOST-ESM, MIROC6, MPI-ESM1-2-HR, MPI-ESM1-2-LR, MRI-ESM2-0, NESM3, NorESM2-LM, NorESM2-MM, TaiESM1	Eyring et al. 2016; O'Neill et al. 2016	For validating the CESM1-simulated total changes
PAMIP	CESM1-WACCM-SC, HadGEM3-GC31-MM, NorESM2-LM	Smith et al. 2019	For validating the CESM1-simulated changes in response to Arctic sea ice loss and associated AA

In this study, we mainly analyzed the response averaged over the 20 years around $4 \times CO_2$. The change patterns averaged over a longer 50-yr period around $4 \times CO_2$ or the 20 years around $2 \times CO_2$ and $8 \times CO_2$ are qualitatively similar and thus not shown. This implies only small impacts of internal variability on the 20-yr averaged v changes shown below. We focused on the boreal cold season from October to March, when Arctic sea ice loss has the greatest impact on Arctic temperatures (Dai et al. 2019), although the changes in the other months are also examined.

We also analyzed monthly data from historical (1970–99) and SSP5–8.5 (2070–99) simulations from 36 CMIP6 models (Table 1) to confirm the overall response to GHG-induced global warming seen in the CESM1 simulations. A multimodel mean was obtained by averaging evenly across all 36 CMIP6 models (we used one realization per model) after interpolating the original model fields onto a common 2.5° latitude × 2.5° longitude grid.

To validate the CESM1-simulated effect of AA and concurring Arctic sea ice loss, we also analyzed four experiments from PAMIP (Smith et al. 2019), which aim to quantify the effect of Arctic sea ice loss (and the associated AA). First, we analyzed two experiments with coupled ocean–atmosphere models (OAGCMs), including an experiment (pa-futArcSIC) constrained by future Arctic SIC and an experiment (pa-pdSIC) constrained by present-day (1979–2008) Arctic SIC climatology from the Hadley Centre Sea Ice and Sea Surface Temperature dataset (HadISST; Rayner et al. 2003). The future SIC is the averaged SIC over 30 years when its global-mean surface air temperature is 2°C warmer than the preindustrial period under a high emissions scenario. The internal SIC is nudged to the current or future SIC with a strong relaxation time scale of one day. In both experiments, radiative forcing is set to the condition at year 2000. We also examined a parallel pair of experiments using atmospheric models (AGCMs) that are similar to the OAGCM experiments but with prescribed sea surface temperatures (SSTs): one experiment (pdSST-futArcSIC) forced with future Arctic SIC, present-day Antarctic SIC, and present-day global SST, and the other experiment (pdSST-pdSIC) forced with present-day global SIC and SST. The pdSST-futArcSIC experiment uses future SST in the areas with more than 10% SIC loss. The use of the present-day SSTs in these AGCM experiments will significantly dampen atmospheric responses to the specified Arctic sea ice losses. Present-day SIC/SST, future SIC, and radiative forcing prescribed in the AGCM experiments are the same as those in the OAGCM experiments, which allows us to approximately isolate the effect of atmosphere–ocean coupling, giving the caveat of the dampened response in the AGCM experiments. Monthly data were available from three models for the above PAMIP experiments (Table 1). For each experiment by each model, there are 100 ensemble runs of 14 months (from 1 April to 31 May of next year) started from different initial conditions. Ensemble means are used to represent the response to Arctic sea ice loss (and associated AA). More information on the PAMIP experiments can be found in Smith et al. (2019).

The statistical significance of the change or difference was assessed using a two-tailed Student's t test at each grid point. The changes in CESM1 1%CO_2 and FixedIce runs were tested with the null hypothesis that the mean of the change relative to the CTL climatology is not different from zero. As for the difference between the 1%CO_2 and FixedIce runs, the null hypothesis was that the means of their changes are equal. The null hypothesis for CMIP6 simulations was that the change from the 1970–99 mean to the 2070–99 mean is zero. For PAMIP experiments, the null hypothesis was that the means of the ensembles are equal.

b. Zonal wave analyses

A spherical harmonic analysis was applied to decompose the v changes into zonal wavenumbers at each latitude on 300- and 850-hPa levels, as done previously for the upper-tropospheric v changes over the Northern Hemisphere (Simpson et al. 2016; Wills et al. 2019). For a given latitude and a pressure level, zonal variations in v can be decomposed into a number of harmonic waves with different zonal wavelengths using a fast Fourier transform. More details can be found in Wills et al. (2019).

c. Layer-mean temperature and geostrophic balance

Airmasses with higher temperature are less dense and occupy more volume, resulting in a thicker layer between the pressure level and the surface and thus a higher altitude at the pressure level. In the free troposphere, the horizontal height gradient force is roughly balanced by the Coriolis term. This allows us to estimate the v wind change using the following geostrophic equation (Holton 2004):

$$v_g = \frac{1}{f}\frac{\partial \Phi}{\partial x} = \frac{g}{f}\frac{\partial Z}{\partial x} = \frac{R}{f}\ln\left(\frac{P_s}{P_1}\right)\frac{\partial \overline{T}}{\partial x}, \quad (1)$$

where v_g is the geostrophic meridional wind, f is the Coriolis parameter, Φ and Z are the geopotential and geopotential height at pressure levels p ($\Phi = Zg$, $g = 9.8\ \mathrm{m\ s^{-2}}$), $p_s = 1000$ hPa, p_1 is 300 or 850 hPa in this study, R is the gas constant of air, and $\overline{T} = \int_{p_1}^{p_s} T d\ln p / \ln(p_s/p_1)$ is pressure-weighted layer-mean temperature. According to Eq. (1), the v_g difference (Δv_g) between two simulations arises from the zonal gradient of their warming difference ($\partial \Delta \overline{T}/\partial x$).

3. Global v change patterns and their effect on v climatology

a. Total v change patterns in response to increased GHGs

Figure 1 shows the October–March mean v change patterns at the 850-hPa (V850) and 300-hPa levels (V300) and vertical pressure velocity change pattern at 500 hPa (ω500) in the CESM1 1%CO_2 run averaged over the 20 years around the time of 4 × CO_2, together with the CTL V850 climatology. As shown in Fig. 1, the tropical v changes imply a low-level meridional convergence and an upper-level meridional divergence over the tropical eastern Pacific, accompanied by enhanced ascending motions. Similar, though weaker, changes are seen over the tropical eastern North Atlantic (Fig. 1). Over the tropical Indian Ocean and eastern Africa, the v changes imply an upper-level meridional convergence and a lower-level meridional divergence coupled with enhanced descending motions (Fig. 1). Thus, the tropical v changes vary with height and tend to be opposite at the lower and upper troposphere, coupled with the changes in vertical motions. The vertical motion changes are associated with an increase in precipitation near the equator over the eastern Pacific and eastern Atlantic and a reduction in precipitation near the equator over the Indian Ocean (not shown). The vertical velocity changes, however, are weak over the extratropics and noticeable mainly over the low latitudes (within 30°S–30°N) (Fig. 1b), where the upper-tropospheric v change is dominated by an upward shift of the rising branch of the Hadley circulation (Dai and Song 2020). Thus, the mid-to-high latitude v changes in both hemispheres are unlikely to be caused or associated with the local changes in vertical motion.

The v changes at both the lower and upper tropospheric levels exhibit a similar wavenumber-4 structure north of 30°N (spatial pattern correlation $r = 0.76$, $p < 0.01$), with southerly or positive anomalies centered around central Eurasia (60°–120°E), the Bering Strait and Alaska, central-eastern North America, and eastern North Atlantic to Atlantic coastal Europe that are separated by northerly or negative anomalies between them (shading in Fig. 1). Alternating, wavelike v change patterns are also seen in the Southern Hemisphere midlatitudes, with a zonal wavenumber-3 structure that differs from those in the Northern Hemisphere but is still broadly comparable at 850- and 300-hPa levels south of 30°S (with a spatial pattern correlation $r = 0.41$, $p < 0.01$). Thus, the v changes are quasi-barotropic (i.e., independent of height) in the extratropics.

The multimodel mean v change patterns in 36 CMIP6 models from 1970–99 to 2070–99 (Figs. 2a,b) are broadly consistent with the CESM1-simulated overall v changes shown in Fig. 1. They have a pattern correlation of 0.48 for V850 and 0.57 for V300 over the globe (both with $p < 0.01$). Over 30°–90°N, the pattern correlation degrades slightly (0.38 for V850 and 0.34 for V300) but remains statistically significant. Some regional differences exist, for instance, over central Russia and northern Mexico, where the CESM1 shows larger biases in the v climatology than the CMIP6 multimodel mean, and the CMIP6 intermodel results revealed some relationship between the simulated v change and its climatology (figure not shown). The CMIP6 multimodel mean change patterns shown in Fig. 2 are comparable to those from CMIP5 projections shown by Simpson et al. (2016), Wills et al. (2019) and Tuel et al. (2021), who did not examine Southern Hemispheric v changes. Substantial differences in v change patterns exist among individual CMIP6 models (circles in Figs. 2c,d). The correlations of v change patterns between CESM1 and CMIP6 multimodel mean, which averages out some extreme model results, generally sit in the upper range of the CMIP6 ensemble spread (Figs. 2c,d). These results suggest that the multimodel ensemble mean v changes in CMIP6 models are stable and broadly similar to the CESM1-simulated v change patterns, while large intermodel differences exist, especially over the northern extratropics.

The ascent and descent changes in CMIP6 models (contours in Fig. 2b) also broadly match those in the CESM1 simulation ($r = 0.52$, $p < 0.01$). They are consistent with the tropical precipitation changes with increased precipitation along the equator over the Pacific and Atlantic and in the northern tropical Indian Ocean under global warming (Geng et al. 2020), which is related to the zonal contrasting tropical SST changes and interhemispheric heating transport (Mamalakis et al. 2021). Thus, the tropical v change pattern in the CMIP6 models (Figs. 2a,b) likely originates from the changes in tropical convection, while the vertical motion changes in the extratropics are rather small and unlikely to fully

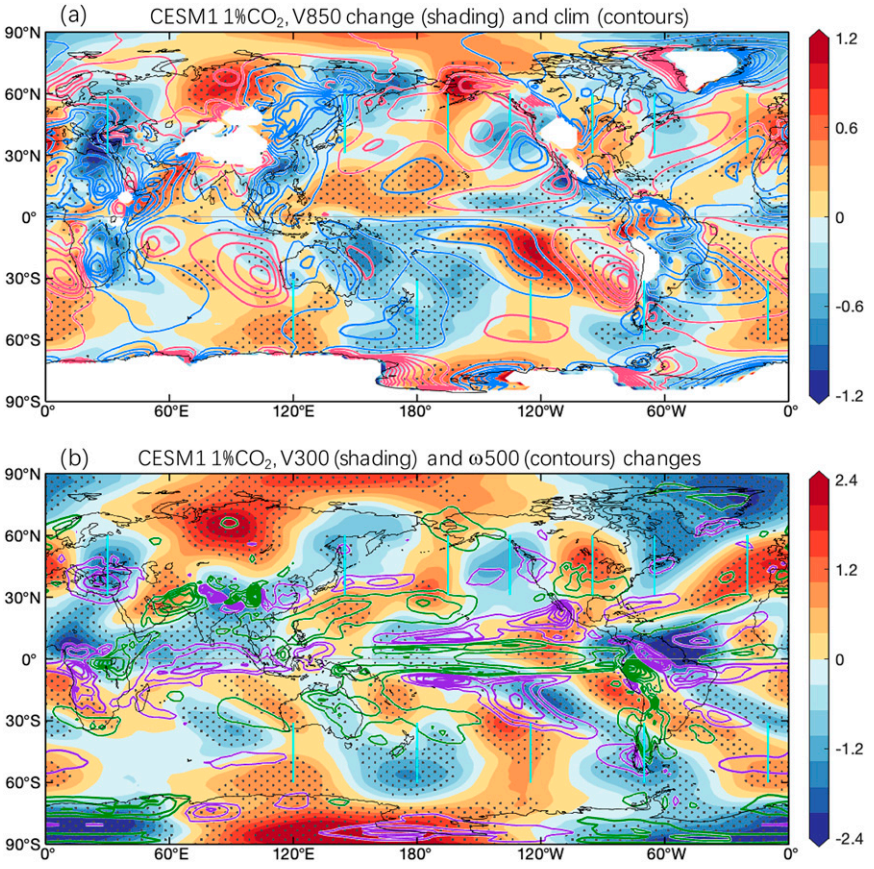

FIG. 1. CESM1-simulated October–March mean changes in v (shading; m s^{-1}) at (a) 850 hPa (V850) and (b) 300 hPa (V300), together with the CTL climatological V850 [contours in (a); interval = 0.5 m s^{-1}, with red lines for positive and blue lines for negative values] and changes in vertical pressure velocity at 500 hPa [ω500; contours in (b), interval = 0.005 Ps s^{-1}, with green lines for ascending and purple lines for descending motion], averaged over the 20 years (years 131–150) around the time of 4 × CO_2 from the 1%CO_2 run. The zero contours are omitted. The changes are relative to CTL climatology. The stippling indicates the v change is significant at the 5% level based on a Student's t test. The cyan lines in (a) and (b) highlight the cross sections close to the centers of the positive and negative V850 changes, which are used in Fig. 8.

explain the strong v changes there, consistent with the CESM1 simulations.

b. *The v change patterns in response to CO_2 forcing and AA alone*

Next, we separate the CESM1-simulated overall v changes into contributions from AA and the effect of increased CO_2 without AA. In the FixedIce run, as the Arctic sea ice loss is largely suppressed (Dai et al. 2019), the Arctic-to-global warming ratio is reduced from ~3 to ~1.4 after the time of 2 × CO_2 (year 70). The Arctic-minus-global warming difference is greatly reduced from 8.19° to 1.29°C (by ~84%) averaged over years 131–150 around the time of 4 × CO_2. Therefore, AA in the FixedIce run caused by other processes (including those over land) besides the effect of sea ice melting is small, as shown previously (Dai et al. 2019; Dai and Song 2020). The v change in the FixedIce run mainly represents the response to the CO_2 forcing alone without the effect from large AA (i.e., Arctic-to-global warming ratio > 1.4), while the 1%CO_2 minus FixedIce difference reflects the effect of AA (and associated sea ice loss) seen in the 1%CO_2. The v change patterns in FixedIce (Figs. 3a,c) are similar to those in the 1%CO_2 run (with a global pattern correlation of 0.86 and 0.91 for the 850- and 300-hPa levels between Fig. 1 and Figs. 3a,c, both with a $p < 0.01$), except for slightly stronger amplitudes over the northern mid-to-high latitudes that result in a change pattern roughly opposite to the response to the CO_2 forcing alone in the 1%CO_2 minus FixedIce difference maps (Figs. 3b,d). In other words, the AA's effect on v partially cancels the v response to the CO_2 forcing alone in the northern mid-to-high latitudes. Moreover, the vertical motion at 500 hPa and thus atmospheric convection is barely affected by AA, and the v changes caused by AA and Arctic sea ice loss are located mainly within 30°–90°N (Figs. 3b,d). Thus, the total v change pattern in the tropics and Southern Hemisphere in the 1%CO_2 run is dominated by the effect of increased CO_2 without AA. North of 30°N, in line with Dai and Deng (2021), we find that

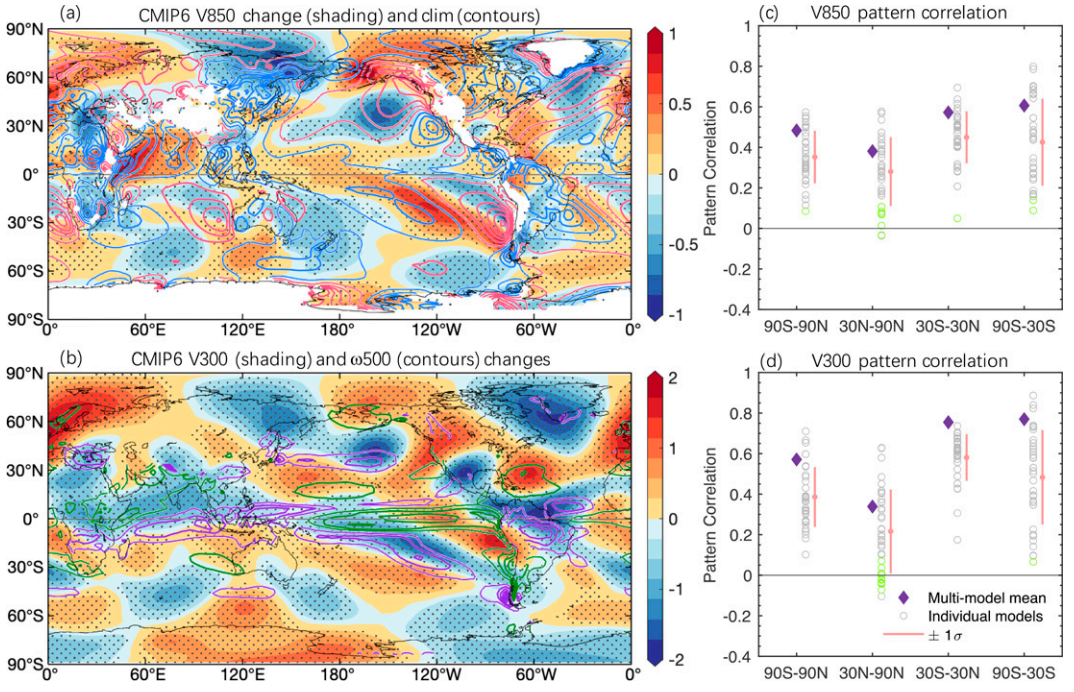

FIG. 2. (left) CMIP6 multimodel mean changes from 1970–99 to 2070–99 in October–March mean (a) V850 and (b) V300 (shading; m s^{-1}) from the all-forcing historical (for 1970–2014) and SSP5–8.5 (for 2015–99) simulations averaged over 36 CMIP6 models, together with the corresponding 1970–99 climatology of October–March mean V850 [contours in (a); interval = 0.5 m s^{-1}, with red lines for positive and blue lines for negative values] and changes in pressure velocity at 500 hPa [ω500; contours in (b), interval = 0.005 Ps s^{-1}, with green lines for ascending and purple lines for descending motion]. The zero contours are omitted. The stippling indicates the change is significantly different from zero at the 5% level based on a Student's *t* test. (right) Spatial pattern correlations between the CESM1-simulated *v* changes shown in Fig. 1 and the *v* changes from CMIP6 multimodel mean (purple diamonds) or individual models (circles) over 90°S–90°N, 30°–90°N, 30°S–30°N, and 30°–90°S at (c) 850 and (d) 300 hPa. The circles in gray (green) are for significant (insignificant) correlations at the 5% level based on a Student's *t* test. The pink line indicates the ±1 standard deviation range of the circles.

AA and CO_2 forcing alone produce *v* change patterns with opposite phases, with AA's effect weakening the other effect of increased CO_2 on the *v* wind.

The *v* changes in the 1%CO_2 and FixedIce runs and the 1%CO_2 minus FixedIce *v* differences are decomposed according to the zonal wavenumber (WN) (Fig. 4). For the 1%CO_2 and FixedIce runs (Figs. 4a–d), WN3–5 changes (red, blue, and green contours) dominate the *v* changes over the northern midlatitudes, while WN1–2 changes (black contours) are mainly over the Arctic and Antarctic and WN > 5 changes (yellow contours) are mainly over the tropics. Over 30°–60°N, the strongest changes are seen at WN4 (blue contours in Figs. 4a–d). The WN4 changes share similar positive and negative centers with the total *v* change patterns shown in Figs. 1 and 2a,b. In the northern midlatitudes, the WN4 changes in the 1%CO_2 run exhibit weaker magnitudes than that in the FixedIce run (Figs. 4a–d), resulting in a WN4 pattern of the 1%CO_2 minus FixedIce *v* difference (Figs. 4e–f) that has opposite phases compared with the WN4 change pattern due to increased CO_2 alone.

As a result, in the upper troposphere, the intermediate-scale waves (WN4–6) prevailing in the Northern Hemispheric subtropics (contours in Fig. 5d) show some weakening of WN6 but strengthening of WN4–5 in the 1%CO_2 run (shading in Fig. 5d), in line with Simpson et al. (2016) and Wills et al. (2019). In the lower troposphere, where the intermediate-scale waves and their zonal scale lengthening are not evident, *v* changes are greater at northern high latitudes than at lower latitudes in the 1%CO_2 and FixedIce runs and their differences (Figs. 5a–c). For the 1%CO_2 run, there is a pronounced strengthening of WN3–4 waves over 40°–80°N for V850 (Fig. 5a). Further analysis reveals that all the above changes are mainly dominated by the effect of increased CO_2 without AA (Figs. 5b,e), while AA generally leads to an opposite effect, weakening the change magnitudes (Figs. 5c,f). A notable exception is at WN3–4 in the northern midlatitudes and at WN1–2 at the northern high latitudes, where AA is strong enough to reduce or overwhelm the direct effect of increased CO_2 without AA (Figs. 5b,c,e,f). The strengthening of WN3 waves in the southern midlatitudes is seen in both the lower and upper troposphere (Figs. 5a,d), with identical magnitudes in the 1%CO_2 and FixedIce runs (Figs. 5b,e), indicating a minimal effect of AA on the Southern Hemispheric *v* changes.

The *v* change averaged over the three PAMIP models shows a WN4 pattern over the northern mid-to-high latitudes

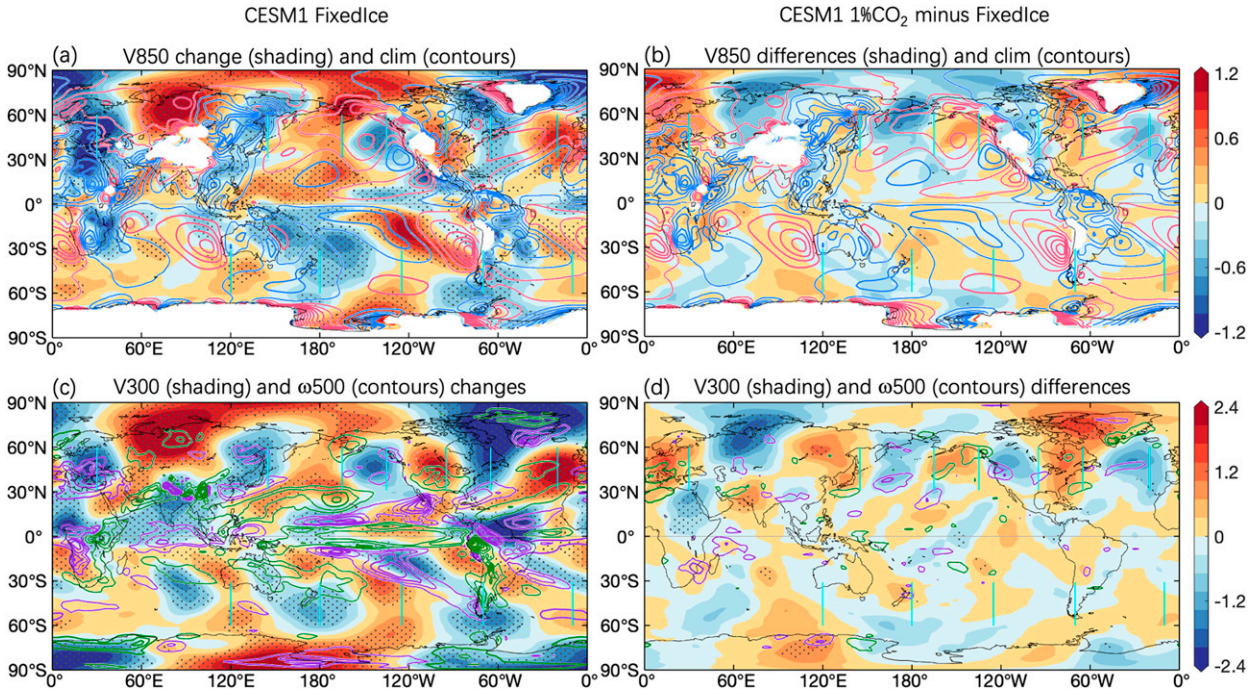

FIG. 3. CESM1-simulated October–March mean (left) v changes (shading; m s^{-1}) from the FixedIce run relative to CTL climatology and (right) 1%CO_2 minus FixedIce v difference (shading; m s^{-1}) at the (a),(b) 850-and (c),(d) 300-hPa levels averaged over the 20 years (years 131–150) around 4 × CO_2. Contours in (a) show the CTL climatological V850 (interval = 0.5 m s^{-1}, with red lines for positive and blue lines for negative values), and contours in (b) show the changes in pressure velocity at 500 hPa (ω500; interval = 0.005 Ps s^{-1}, with green lines for ascending and purple lines for descending motion). The zero contours are omitted. The cyan lines are as in Fig. 1. The stippling indicates the change or difference is significant at the 5% level based on a Student's t test.

in the OAGCM experiments (Figs. 6a,b), broadly consistent with the CESM1-simulated AA-induced v change pattern (Figs. 3b,d). Their global pattern correlations are 0.43 for V850 and 0.45 for V300 (both with $p < 0.01$). Pattern correlations are higher over 30°–60°N, where the magnitudes of WN4 changes are large ($r = 0.62$ for V850 and $r = 0.69$ for V300). The individual PAMIP models also show similar changes over the northern mid-to-high latitudes, although there are some regional discrepancies among them, especially south of 30°N where the response to Arctic sea ice loss is weak (Figs. 6c–h). The v change pattern becomes weaker in the PAMIP AGCM experiments (not shown) due to the strong dampening effect from the use of fixed SSTs in such experiments. The coupled OAGCM experiments avoid the use of fixed SSTs that dampen atmospheric responses to any forcing, and the atmosphere–ocean interactions may enlarge the atmospheric response, both leading to a stronger atmospheric response to Arctic sea ice loss compared with AGCM simulations (Deser et al. 2016; Smith et al. 2017). As the PAMIP experiments analyzed here are single-year ensemble simulations, oceanic processes that take several years or longer are excluded In contrast, the CESM1 simulations ran continuously over hundreds of years with full dynamical ocean processes. Even so, the v change patterns induced by the Arctic sea ice loss (and the associated AA) are comparable over the northern mid-to-high latitudes between the CESM1 runs and PAMIP OAGCM experiments, suggesting that such a v change pattern does not involve long-term oceanic processes.

Having confirmed the CESM1-simulated overall v change patterns in response to CO_2 forcing using the CMIP6 simulations and the v change patterns in response to Arctic sea ice loss and the associated AA using the PAMIP experiments, we examine CESM1-simulated v response in more detail. We focus on the v change pattern over the extratropics as the tropical v changes are tightly related to the GHG-induced convection and pressure velocity changes, as described above. Figure 7 shows the seasonal variation of the v changes at 850 and 300 hPa averaged over 30°–60°N and 30°–60°S around the time of 4 × CO_2 in the 1%CO_2 and FixedIce runs, together with their difference. The WN4 pattern over 30°–60°N is most pronounced in the boreal cold season and stronger in the FixedIce than 1%CO_2 run, with the largest changes in December in both runs and small changes from September–October (Figs. 7a–c, g–i). In both the 1%CO2 and FixedIce runs, the v changes around the western coast of North America persist throughout the year, whereas in other regions the warm-season v change pattern over 30°–60°N differs from those in the cold season, with broader anomalies (thus fewer wavenumbers) that are often out of phase with those in the cold season.

Based on the v change pattern in the boreal cold season, we select seven cross sections over 30°–60°N and five cross sections over 30°–60°S (marked by the cyan lines in Figs. 1 and 3) to examine its vertical variations (Fig. 8). Generally, the v

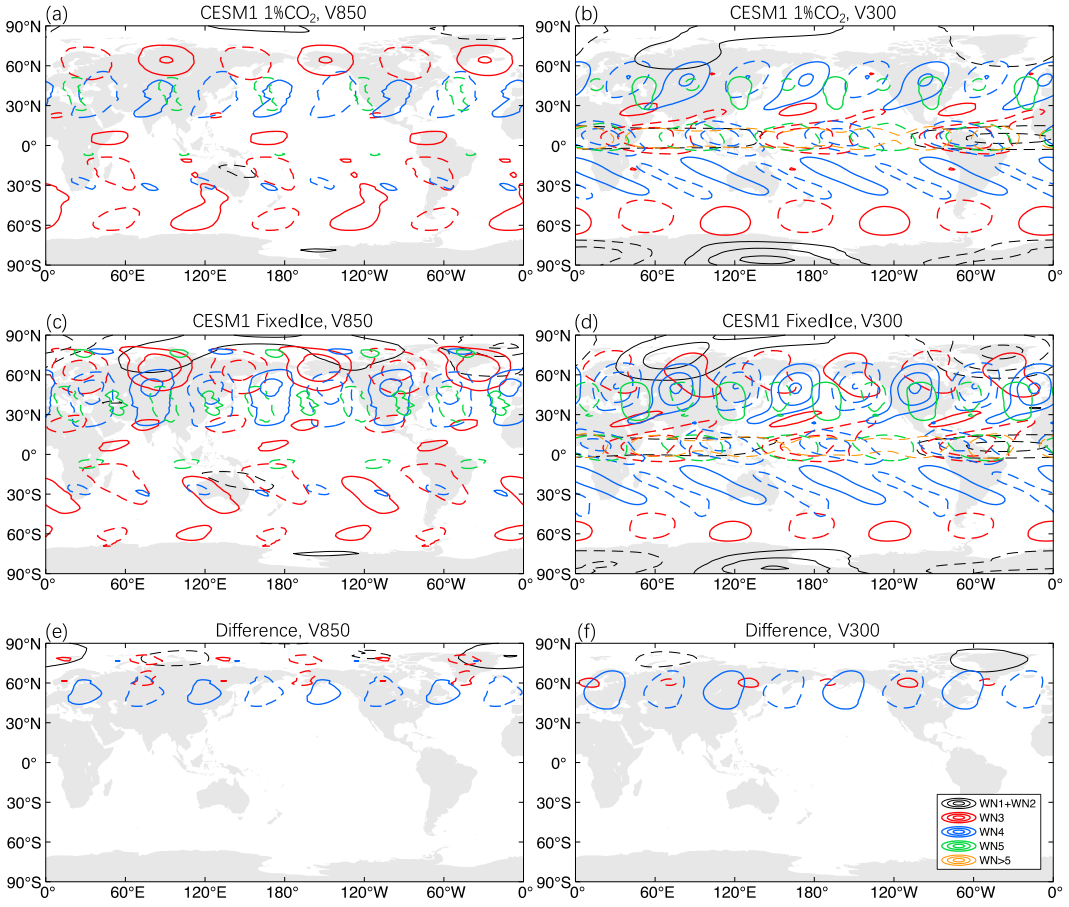

FIG. 4. Zonal wavenumber (WN) decomposition of the CESM1-simulated October–March mean v changes from the (a),(b) 1%CO_2 and (c),(d) FixedIce runs relative to CTL climatology and (e),(f) 1%CO_2 minus FixedIce v difference at the (left) 850- and (right) 300-hPa levels averaged over the 20 years (years 131–150) around 4 × CO_2. The contour intervals are 0.25 and 0.5 m s^{-1} in the left and right panels, respectively, with solid lines for positive and dashed lines for negative values (the zero contours are omitted). Black contours denote the sum of WN 1 and WN2 changes (WN1 + WN2), red contours denote WN3 changes, blue contours denote WN4 changes, green contours denote WN5 changes, and yellow contours denote the changes with WN greater than 5 (WN > 5).

change is small near the surface and has the same sign above 850 hPa for both the 1%CO_2 and FixedIce runs and their difference at all of the cross sections (Fig. 8). The v change strengthens from the surface to a peak around 300–250 hPa and then weakens from 250 to 100 hPa for most cross sections. In the Northern Hemisphere, the v change in FixedIce (due to CO_2 forcing alone without large AA) is generally greater than that in the 1%CO_2 run (which includes the effects from both the CO_2 forcing and AA), resulting in an opposite sign for the 1%CO_2 minus FixedIce difference (which represents the effect of AA) at most of the locations (Fig. 8a–g). One exception is over the central North Pacific, where the v change in the 1%CO_2 run is larger than the FixedIce run in the upper troposphere, leading to a difference with the same sign (Fig. 8c). For the other Northern Hemispheric cross sections, the effect of AA weakens the v change directly induced by the CO_2 forcing alone by 5%–60%, but it is small at the Southern Hemisphere locations as expected since the Arctic is far away from the Southern Hemisphere (Figs. 8h–l). Thus, while the v responses tend to peak around 300–200 hPa, they are quasi-barotropic (i.e., with the same sign) through the troposphere; the effect of AA is to weaken the v response to the CO_2 forcing alone, leading to reduced v changes in the overall response seen in the 1%CO_2 run (consistent with Figs. 1 and 3).

c. *Impact on v climatology*

Here we examine how the v changes mentioned above affect the current v climatology, since it is the sum of the current v and its change that directly affects future meridional advections. The contours in Fig. 1a show the CTL v climatology at 850 hPa over the globe. The v climatological pattern is quasi-barotropic in the extratropics especially north of 30°N but has opposite signs in the upper and lower troposphere in the tropics (not shown). Forced by topography and diabatic heating, the v climatological pattern over the northern mid-to-high latitudes

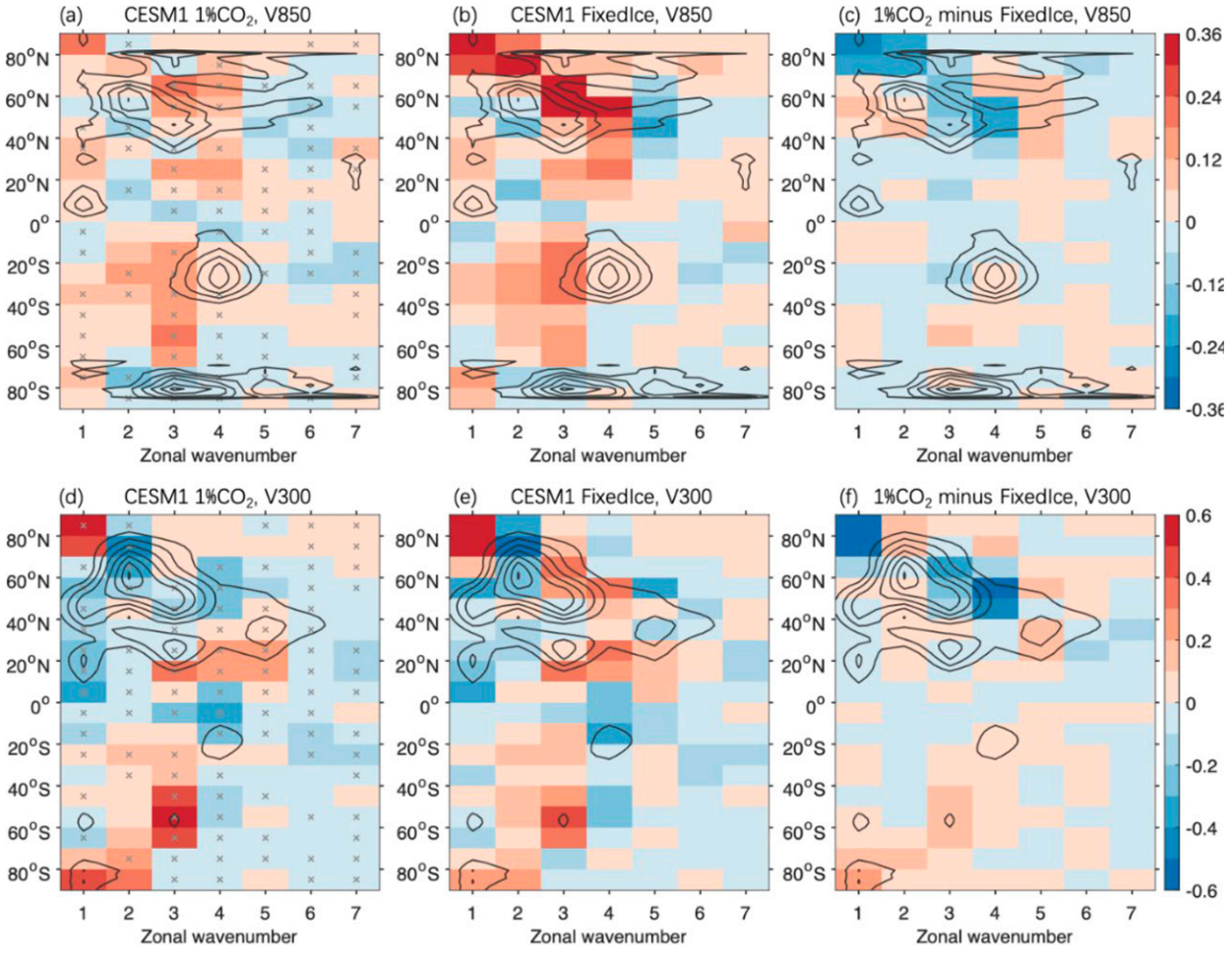

FIG. 5. Root-mean-square amplitudes (shading; m s^{-1}) of the CESM1-simulated October–March (a)–(c) V850 and (d)–(f) V300 changes averaged over 10° latitude as a function of latitude and zonal wavenumber of the v change pattern for the (left) 1%CO_2 and (center) FixedIce runs and (right) 1%CO_2 minus FixedIce v difference averaged over the 20 years (year 131–150) around 4 × CO_2. The changes are relative to the CTL climatology [shown by contours starting from 1 m s^{-1} with an interval of 0.4 m s^{-1} for (a)–(c) and starting from 0.6 m s^{-1} with an interval of 0.24 m s^{-1} for (d)–(f)]. In (a) and (d), the gray cross denotes the region where the CMIP6 multimodel mean change from 1970–99 to 2070–99 agrees on the sign of the CESM1-simulated change.

exhibits a zonal wavenumber-3 (WN-3) pattern, with northerly (negative) centers over Europe, East Asia, and interior North America and southerly (positive) centers between them (Fig. 1a). In the southern mid-to-high latitudes, the v climatology is rather weak but also has three southerly (positive) centers over the eastern South Atlantic, eastern south Indian Ocean, and eastern South Pacific and northerly (negative) anomalies between them (Fig. 1a).

The global pattern correlations between the current V850 climatology (contours in Fig. 1a) and the V850 changes in the 1%CO_2 (shading in Fig. 1a; $r = 0.27$) and FixedIce (shading in Fig. 3a; $r = 0.22$) runs are significantly positive (both with a $p < 0.01$) but not high. This is because the current mean southerly (northerly) v wind at 850 hPa is enhanced by the v change over central Eurasia, Alaska, the central North Pacific, and the central-eastern North Atlantic (East Asia, northern Africa and the Mediterranean region, southern Africa, and most of South America), but the future v change weakens the current v wind over northern Europe, eastern Siberia, and around North America. Apart from the regions with weak climatological V850 (i.e., weaker than 1 m s^{-1}), the strengthening in V850 is particularly prominent over the Mediterranean region and Alaska (both by ~30%), southern Africa (by ~20%), and South America (by ~15%) in the 1%CO_2 run, and it is even stronger in the FixedIce run. The current southerly over central Russia is also projected to strengthen, but the CESM1 tends to overestimate the v change there compared with CMIP6 models (Figs. 1a and 2a).

Correspondingly, the change patterns of the meridional advection of temperature $[-v(\partial T/\partial y)]$ and specific humidity $[-v(\partial q/\partial y)]$ are similar to the v change pattern in the 1%CO_2 and FixedIce runs and their difference, with WN4 (WN3) structure in the northern (southern) mid-to-high latitudes (Fig. 9). As the changes of meridional temperature gradient

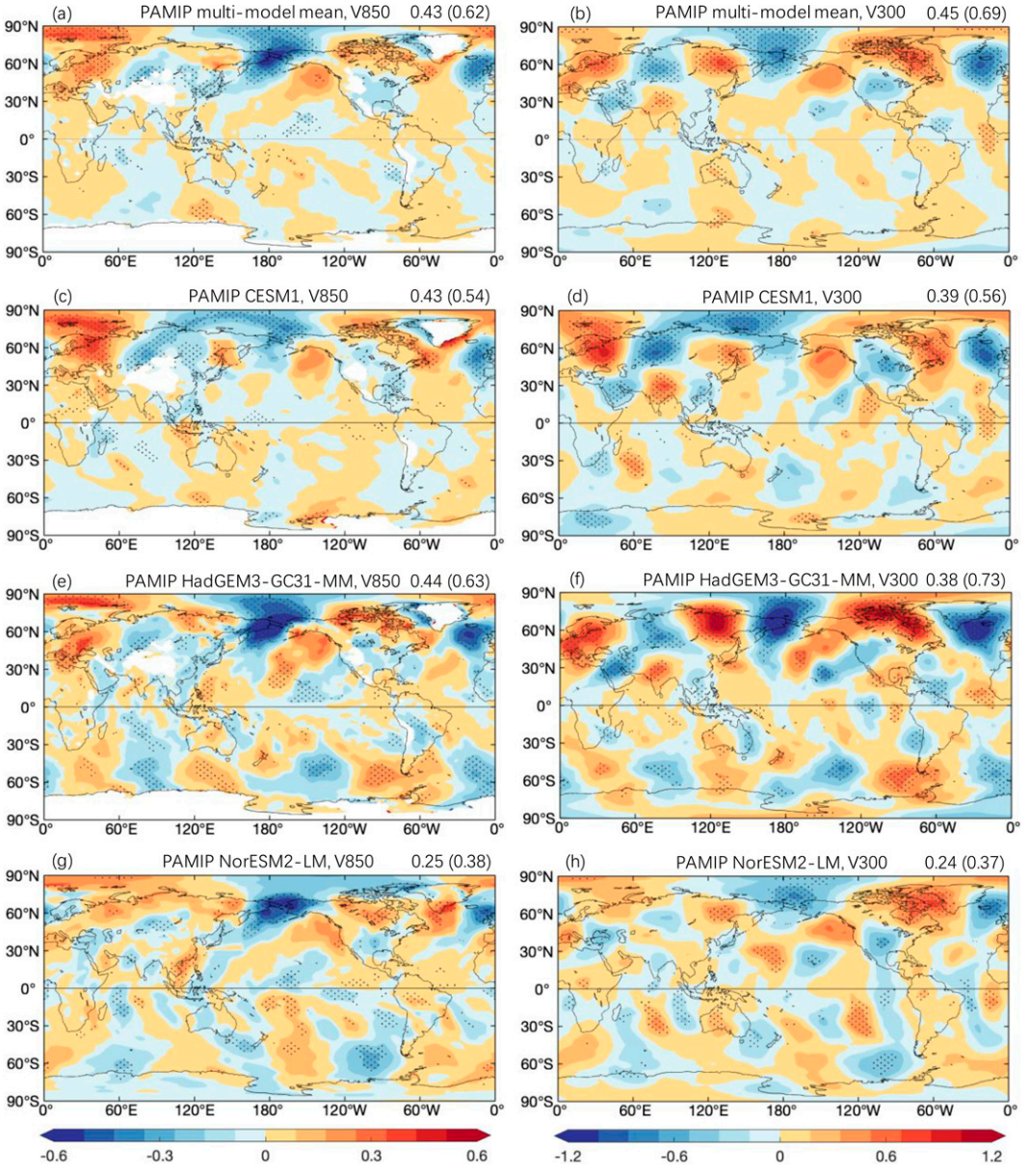

FIG. 6. Ensemble-mean October–March mean (left) V850 and (right) V300 changes (m s^{-1}) in response to Arctic sea ice loss from the PAMIP OAGCM experiments for (a),(b) three-model mean, (c),(d) CESM1, (e),(f) HadGEM3-GC31-MM, and (g),(h) NorESM2-LM. The stippling indicates the change is significant at the 5% level based on a Student's t test. Their pattern correlation over the globe (30°–60°N) with the CESM1-simulated 1%CO_2 minus FixedIce v difference shown in Figs. 3b,d is given at the top right.

and meridional specific humidity gradient are overall small and zonally symmetrical, v changes contribute significantly to the change patterns in meridional heat and moisture transport. The change pattern in 850 hPa $-v(\partial q/\partial y)$ has a positive correlation with its current climatology in both the 1%CO_2 ($r = 0.47$) and FixedIce runs ($r = 0.48$, both with a $p < 0.01$) over the globe, suggesting a strengthening in meridional moisture transport. As shown in Figs. 9a and 9b, strengthened $-v(\partial q/\partial y)$ is evident over Europe, western-central North America, and most southern latitudes in the 1%CO_2 and FixedIce runs. On the other hand, the change in $-v(\partial T/\partial y)$ has a weak and negative global pattern correlation with its climatology in the 1%CO_2 ($r = -0.21$, $p < 0.01$) and FixedIce runs ($r = -0.06$). Over northern mid-to-high latitudes, the $-v(\partial T/\partial y)$ change generally shows an opposite sign with its climatology (Figs. 9d,e), indicating a weakening of meridional heat transport in most northern mid-to-high-latitude regions. This is consistent with Dai and Deng (2021), who found that a pattern correlation of −0.54 over 40°–90°N between $-v(\partial T/\partial y)$ climatology and its change in the CESM1 1%CO_2 run.

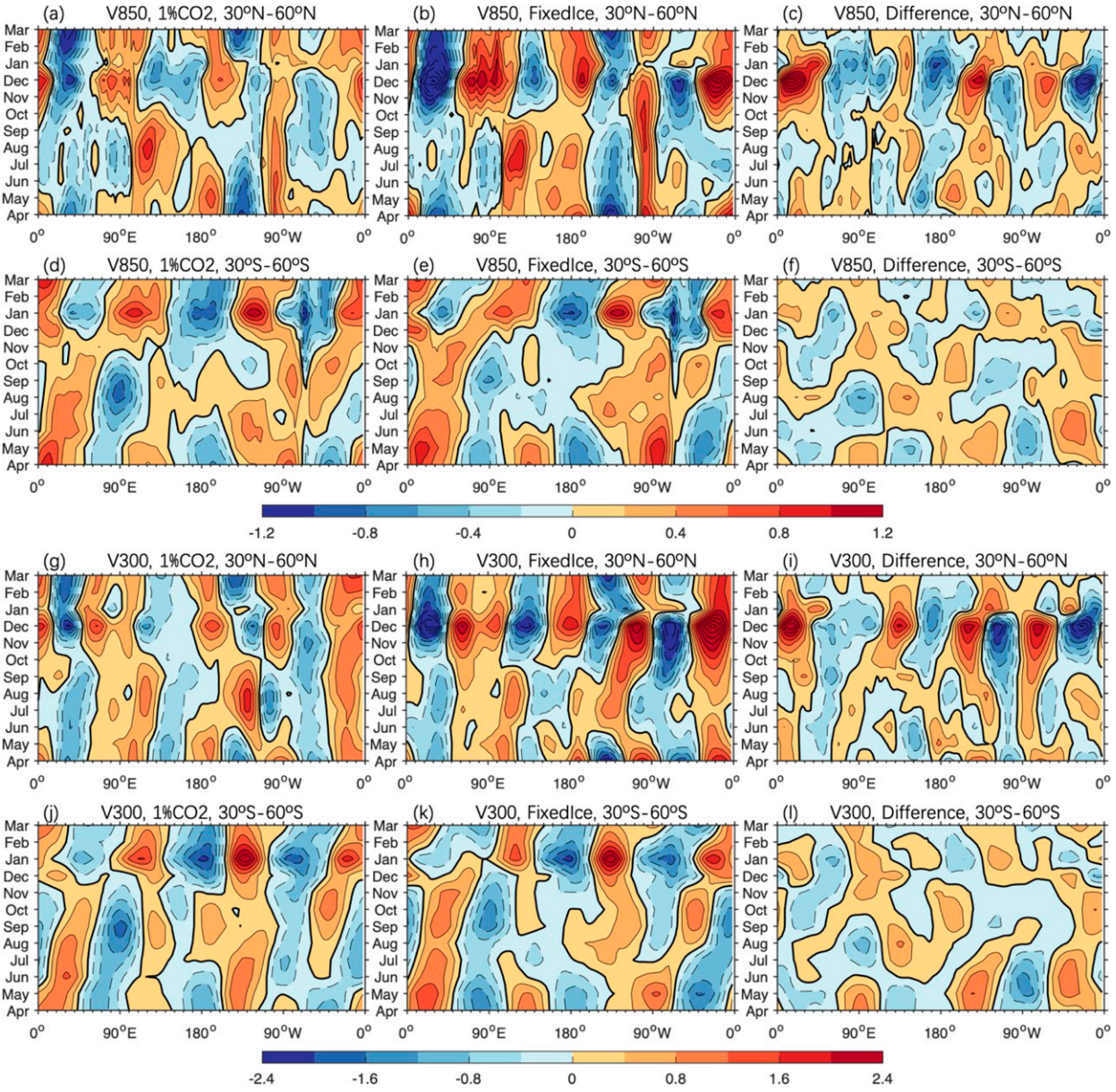

FIG. 7. CESM1-simulated 3-month moving-averaged (a)–(f) V850 and (g)–(l) V300 changes (m s^{-1}; relative to the CTL climatology) averaged over 30°–60°N in (a)–(c) and (g)–(i) and 30°–60°S in (d)–(f) and (j)–(l) as a function of month and longitude during the 20 years (years 131–150) around the time of 4 × CO_2 in the (left) 1%CO_2 and (center) FixedIce runs and (right) the 1%CO_2 minus FixedIce difference.

When averaged over the 30°–60°N/S zones, the CTL v climatology over both zones is modified only slightly by the v changes (Fig. 10). The zonal variance of the CTL v climatology increases only by ~10% in the 1%CO_2 and FixedIce runs (slightly larger in the latter), and the AA-induced variance change is even smaller (~3%). However, large local impacts should be noted. Both the 1%CO_2 and FixedIce runs reveal an eastward shift (by ~5° longitude) and a significant strengthening (by ~1 m s^{-1}) of the northerly CTL v climatology over central Europe (Figs. 1a, 3a, and 10a,b,g,h). In addition, the northerly CTL v climatology around North America (over East Asia) is weakened (strengthened) by the future v change but only by ~0.4 m s^{-1} (~0.3 m s^{-1}) (Figs. 10a,b,g,h). Over 30°–60°S, the v climatology is strengthened slightly (by ~0.15 m s^{-1}) in both the 1%CO_2 and FixedIce runs, with little influence from AA and Arctic sea ice loss (Figs. 10d–f and 10j–l). Overall, the 30°–60°S averaged v change is about a factor of 4 weaker than the current v climatology, leading to similar mean v winds over most longitudes for the current and future climates in both the 1% CO_2 and FixedIce simulations (Figs. 10d,e,j,k).

The effect from AA and Arctic sea ice loss (shading in the right column of Fig. 10) is even smaller than the v change in the

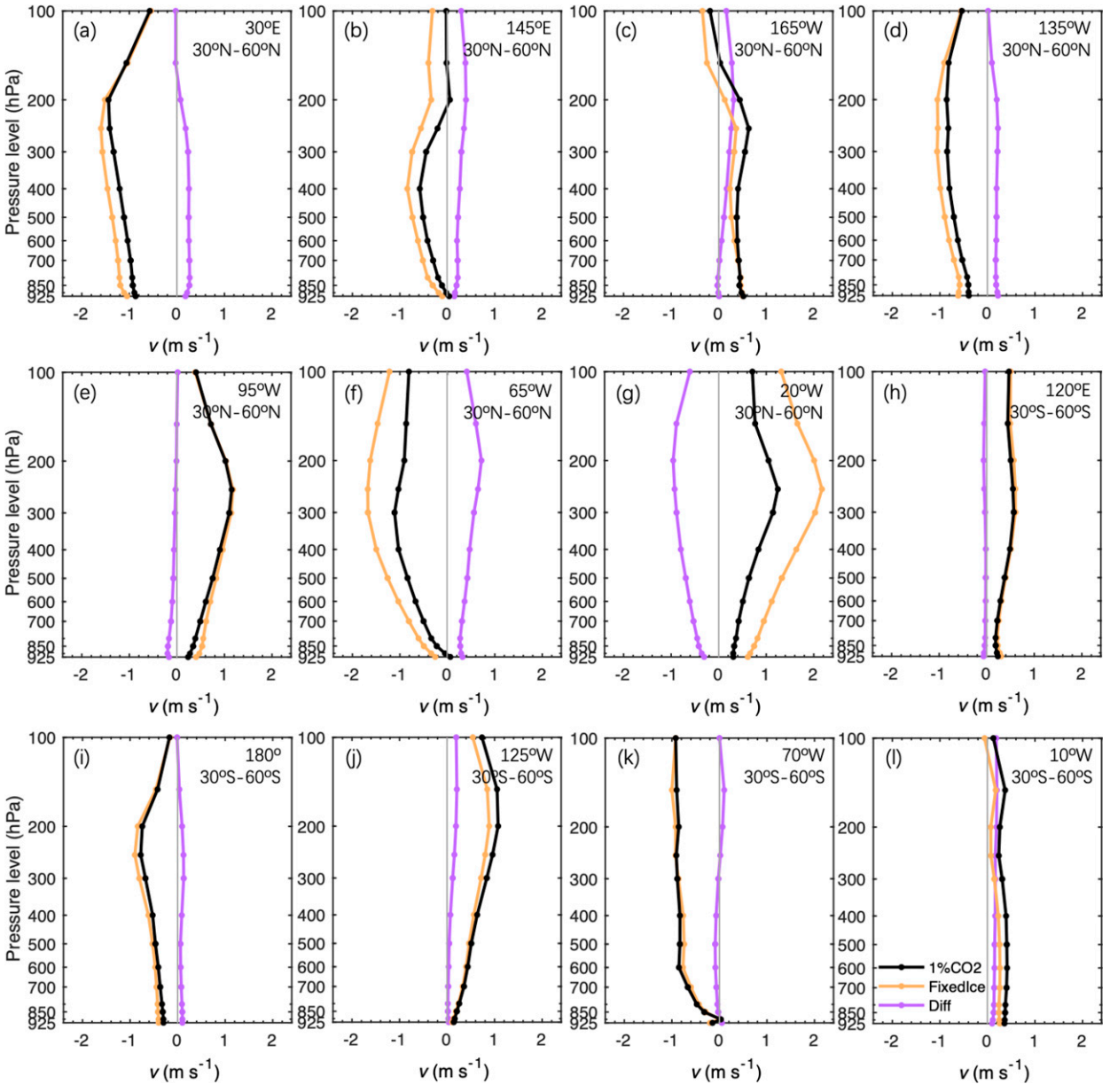

FIG. 8. CESM1-simulated October–March mean v changes (m s^{-1}; relative to CTL climatology) as a function of pressure levels averaged over the 20 years (years 131–150) around 4 × CO_2 from the 1%CO_2 (black lines) and FixedIce runs (orange lines) and the 1%CO_2 minus FixedIce difference (purple lines) averaged over 30°–60°N in (a)–(g) or 30°–60°S in (h)–(l) at selected longitude locations as marked in Fig. 1: (a) 30°E, (b) 145°E, (c) 165°W, (d) 135°W, (e) 95°W, (f) 65°W, (g) 20°W, (h) 120°E, (i) 180°, (j) 125°W, (k) 70°W, and (l) 10°W.

1%CO_2 or FixedIce run, and it generally weakens the current v climatology slightly (≤0.2 m s^{-1} averaged over 30°–60°N) with a global pattern correlation of −0.11 for V850 and −0.25 for V300. The AA-induced v change, however, does not weaken the climatological v everywhere in the northern mid-to-high latitudes. As shown in Fig. 3b, it enhances the current northerly V850 climatology over interior North America and strengthens the current southerly V850 over the eastern North Pacific and western North Atlantic, partially cancelling the response to the increased CO_2 alone (by ~50%). Moreover, AA does not always go against the effect of increased CO_2; for instance, they both lead to negative V850 change over East Asia (110°–125°E, 20°–35°N; Figs. 3a,b), enhancing the current northerly V850 climatology by ~0.3 m s^{-1} (18%) and ~0.2 m s^{-1} (12%), respectively.

As mentioned above, the projected strengthening in climatological northerly v over central Europe shown in Figs. 2a and 11a and previous studies (e.g., Tuel et al. 2021) is mainly due to the effect of CO_2 forcing without AA (Figs. 3 and 10a–c). As can be seen in Fig. 11a, the CMIP6 multimodel

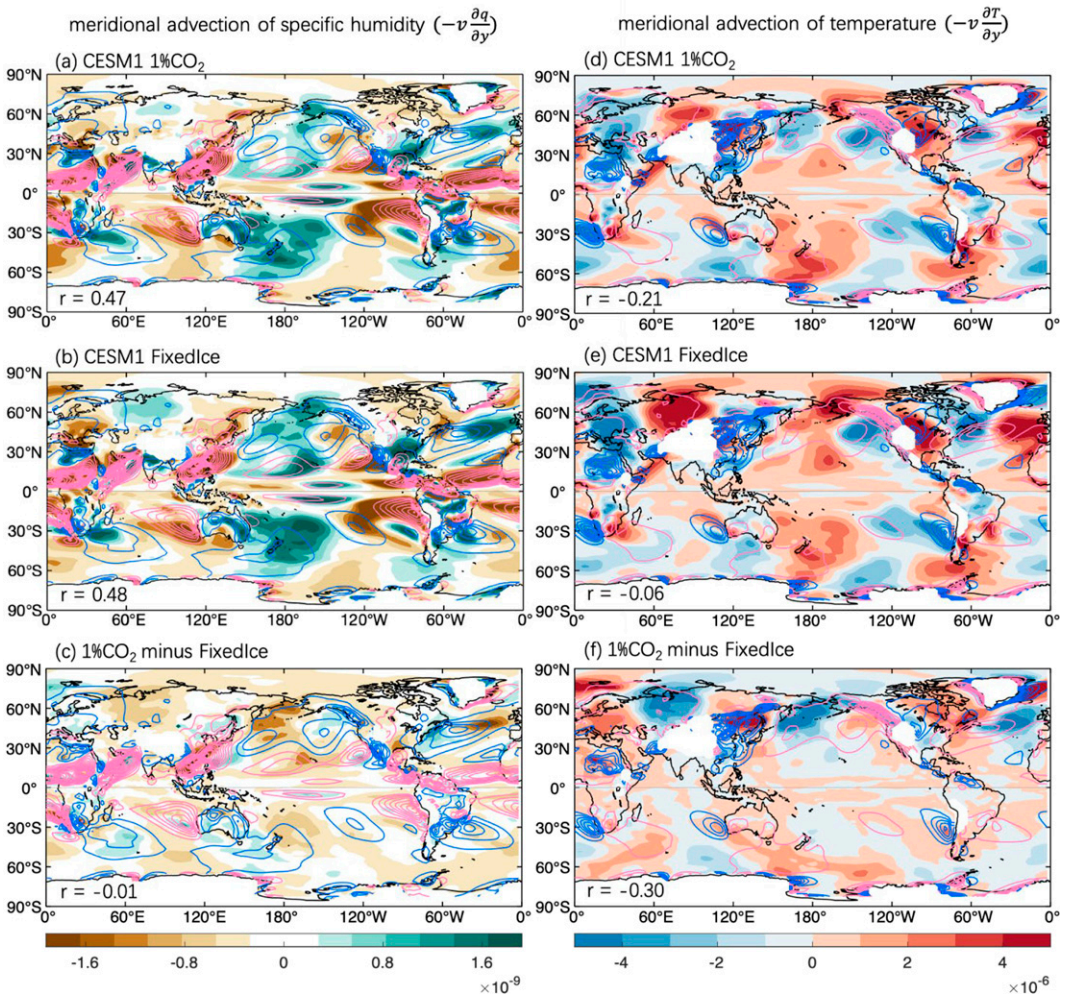

FIG. 9. CESM1-simulated October–March mean changes in meridional advection of (a)–(c) specific humidity $[-v(\partial q/\partial y)$; shading; kg kg^{-1} s^{-1}] and (d)–(f) temperature $[-v(\partial T/\partial y)$; shading; K s^{-1})] at the 850-hPa level averaged over the 20 years (years 131–150) around 4 × CO_2 from the (top) 1%CO_2 and (middle) FixedIce runs, and (bottom) their difference, together with the CTL climatology [contour intervals are 2×10^{-9} kg kg^{-1} s^{-1} and 8×10^{-16} K s^{-1} in (a)–(c) and (d)–(f), respectively, with pink lines for positive and blue lines for negative values; zero contours are omitted]. The pattern correlation coefficient between the contours and shading are shown at the bottom left of each panel.

mean V850 changes over Europe exceed the intermodel standard deviation, whereas the intermodel standard deviation is larger around North America and thus covers the multimodel mean v changes there, indicating a higher signal-to-noise ratio over Europe than around North America, which is consistent with a greater uncertainty in V300 and hydroclimate response in western North America than in the Mediterranean, as demonstrated by Simpson et al. (2016). This is likely due to that the effects from AA and increased CO_2 alone on v are more comparable around North America (Figs. 3 and 10b,c,h,i). In the models with stronger northerly V850 changes over Europe, we see a drier Europe near the end of the twenty-first century, which exacerbates the drying over the Mediterranean region (Figs. 11b,c). However, the strengthened northerly v over Europe will not lead to more cold air outbreaks in the future due to the reduced $\partial T/\partial y$ resulted from Arctic sea ice loss (Dai and Deng 2021) and the local warming caused by shrinking snow cover (Peings et al. 2013). Daily temperature variability and temperature extremes are projected to decrease over the northern midlatitudes (Chen et al. 2019) due to a reduction in $\partial T/\partial y$ and its variance rather than changes in v (Dai and Deng 2021).

4. Impacts of nonuniform warming

This section attempts to explore the causes of the v change patterns over the extratropical regions in response to increased CO_2 and AA alone. Simpson et al. (2016) suggested that the WN5 v change pattern in the northern subtropical upper troposphere, where the zonal-mean westerly winds are strong and act as a waveguide, is due to a shift in the dominant scale of intermediate waves (WN ≥ 4) caused by westerly accelerations.

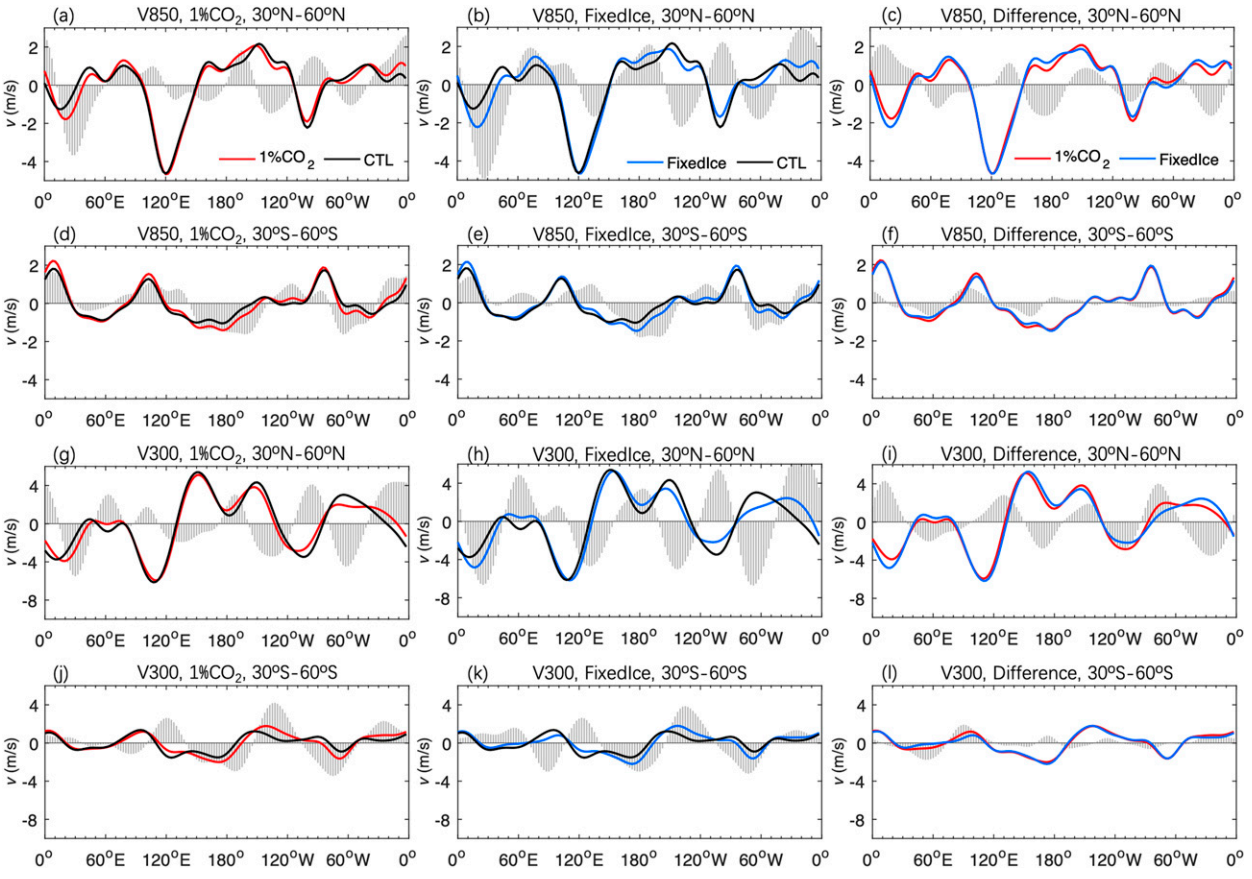

FIG. 10. CESM1-simulated October–March mean (a)–(f) V850 and (g)–(l) V300 averaged over 30°–60°N in (a)–(c) and (g)–(i) and 30°–60°S in (d)–(f) and (j)–(l) during the 20 years (years 131–150) around the time of 4 × CO_2 from the CTL (black), 1%CO_2 (red), or FixedIce (blue) runs, and the difference between the two curves (gray shading; multiplied by a factor of 4).

However, the intermediate waves are not evident in the lower troposphere and the Southern Hemisphere in our CESM1 runs (Figs. 5a,d). Moreover, the v response to increased CO_2 and AA alone on the poleward flank of the subtropical jet is dominated by the WN4 (WN3) pattern (Figs. 4c–f) rather than WN5 pattern. This suggests that the previously proposed mechanism involving jet acceleration and prevalence changes in intermediate waves may not play a major role in the CESM1-simulated

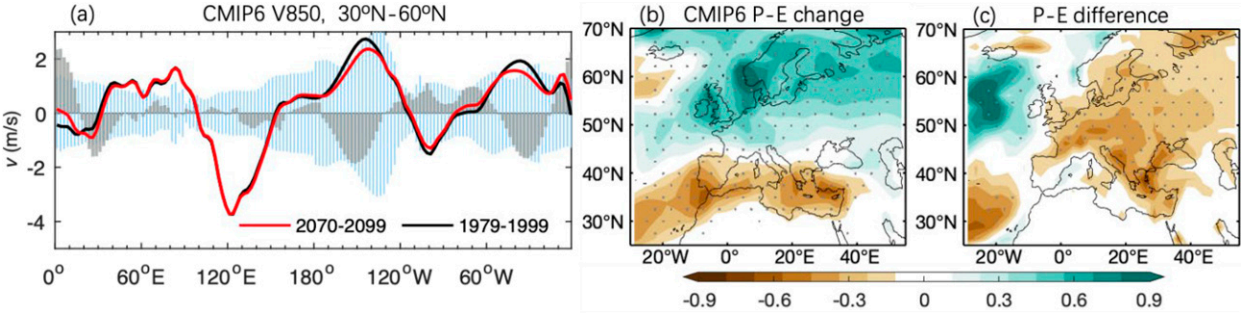

FIG. 11. (a) CMIP6 multimodel mean October–March V850 climatology (m s^{-1}) near the end of the twentieth (black line; 1970–99) and twenty-first centuries (red line; 2070–99) averaged over 30°–60°N, and its change from 1970–99 to 2070–99 (gray bars; multiplied by a factor of 4). Blue vertical lines highlight the ±1 standard deviation range of the changes among the 36 CMIP6 models (also multiplied by a factor of 4). (b) CMIP6 multimodel mean precipitation–evaporation ($P - E$) changes (mm day^{-1}) averaged over October–March from 1970–99 to 2070–99 over Europe and surrounding regions. (c) The differences of the $P - E$ changes (mm day^{-1}) between the 10 CMIP6 models with largest and smallest northerly V850 change averaged over the cross section 30°E, 30°–60°N (shown in Fig. 1). The stippling indicates that the change or difference is significant at the 5% level based on a Student's t test.

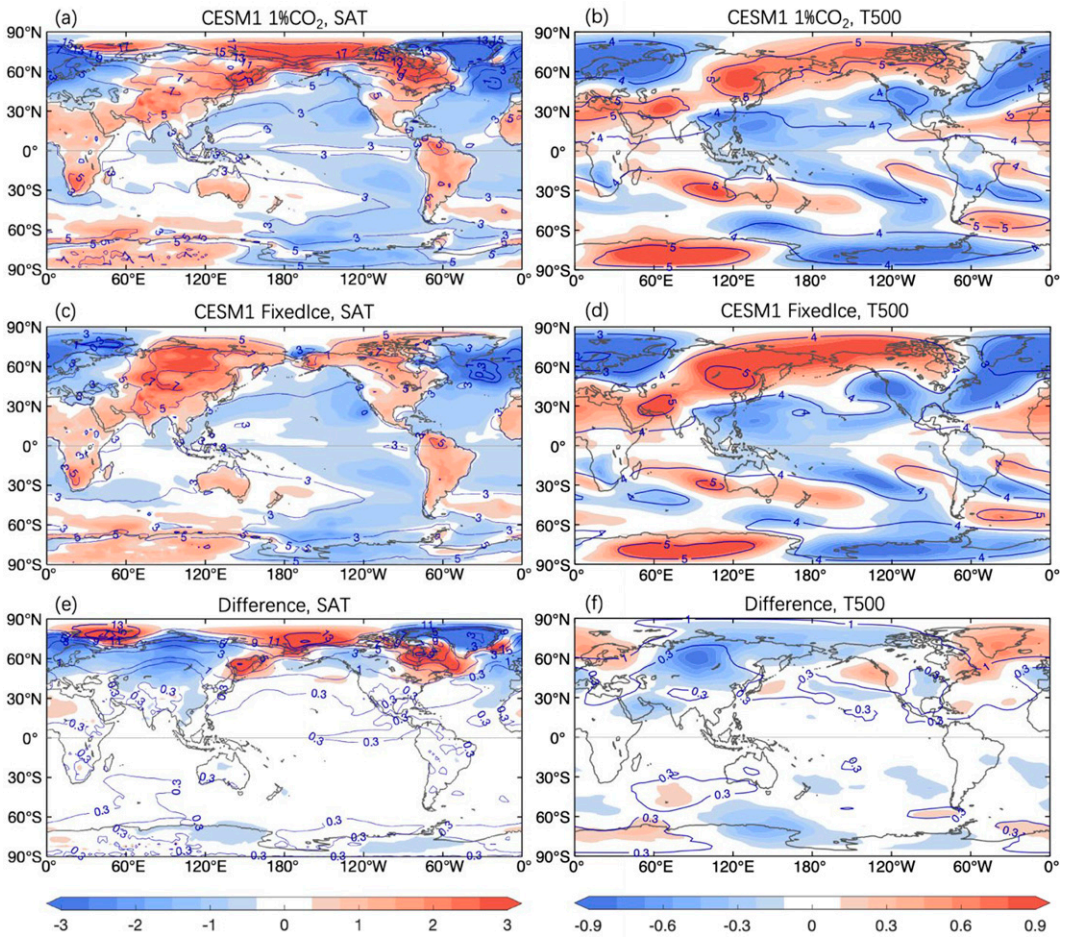

FIG. 12. CESM1-simulated October–March mean change (relative to CTL climatology) in (left) surface air temperature (SAT; contours; K) and its zonal anomalies (shading; deviations from the zonal mean change) and (right) 500-hPa air temperature (T500; contours; K) and its zonal anomalies (shading; deviations from the zonal mean change) averaged over the 20 years (years 131–150) around the time of 4 × CO_2 from the (a),(b) 1%CO_2 and (c),(d) FixedIce runs and (e),(f) the 1%CO_2 minus FixedIce difference.

v responses in the lower troposphere, in the northern mid-to-high latitudes, and the Southern Hemisphere.

The mean v wind pattern also depends on the orography and zonal thermal contrast (Wills et al. 2019). While the orography is fixed, the lower-tropospheric temperature warms unevenly under increasing GHGs due to different surface properties of ocean and land (e.g., more evaporative cooling over oceans and positive surface albedo feedback over land; Joshi et al. 2013), deep-ocean heat uptake and storage (Manabe et al. 1991; Marshall et al. 2015), upper-ocean horizontal heat transport (Dai et al. 2005), and amplified warming associated with Arctic sea ice loss (Dai et al. 2019). With reduced zonal temperature contrast, AGCM simulated a zonal wavenumber-4 geopotential height response in the midtroposphere over the northern midlatitudes during winter (Molteni et al. 2011). The zonal thermal contrast from East Asia to the western North Pacific in the middle and upper troposphere determines the recent changes in the strength of the East Asian summer monsoon, with a large-scale southerly flow over East Asia (Dai et al. 2013). Dai and Deng (2021) found that the v and $\partial T/\partial x$ change patterns at 850 hPa under increased CO_2 are significantly correlated over the Northern Hemisphere mid-to-high latitudes. These findings all suggest that the v change patterns may be partly caused by zonally nonuniform warming.

Figure 12 shows the changes in surface air temperature (SAT) and 500-hPa air temperature in the CESM1 runs and their zonal anomalies (i.e., deviations from the zonal mean change). It is clear that the surface and tropospheric warming is zonally nonuniform, with larger warming over East and South Asia, North America, Africa, and South America but less warming over the oceans at similar latitudes in both the 1%CO_2 and FixedIce runs (Figs. 12a,c). Warming over Europe is below the zonal mean but still larger than that over the North Atlantic Ocean. The temperature zonal anomalies at 500 hPa (Figs. 12b,d) are similar to those for SAT, with a global pattern correlation of 0.51 and 0.65 for the 1%CO_2 and FixedIce runs ($p < 0.01$ for both cases). The SAT changes due to increased CO_2 are similar to the rapid response to CO_2 increases without

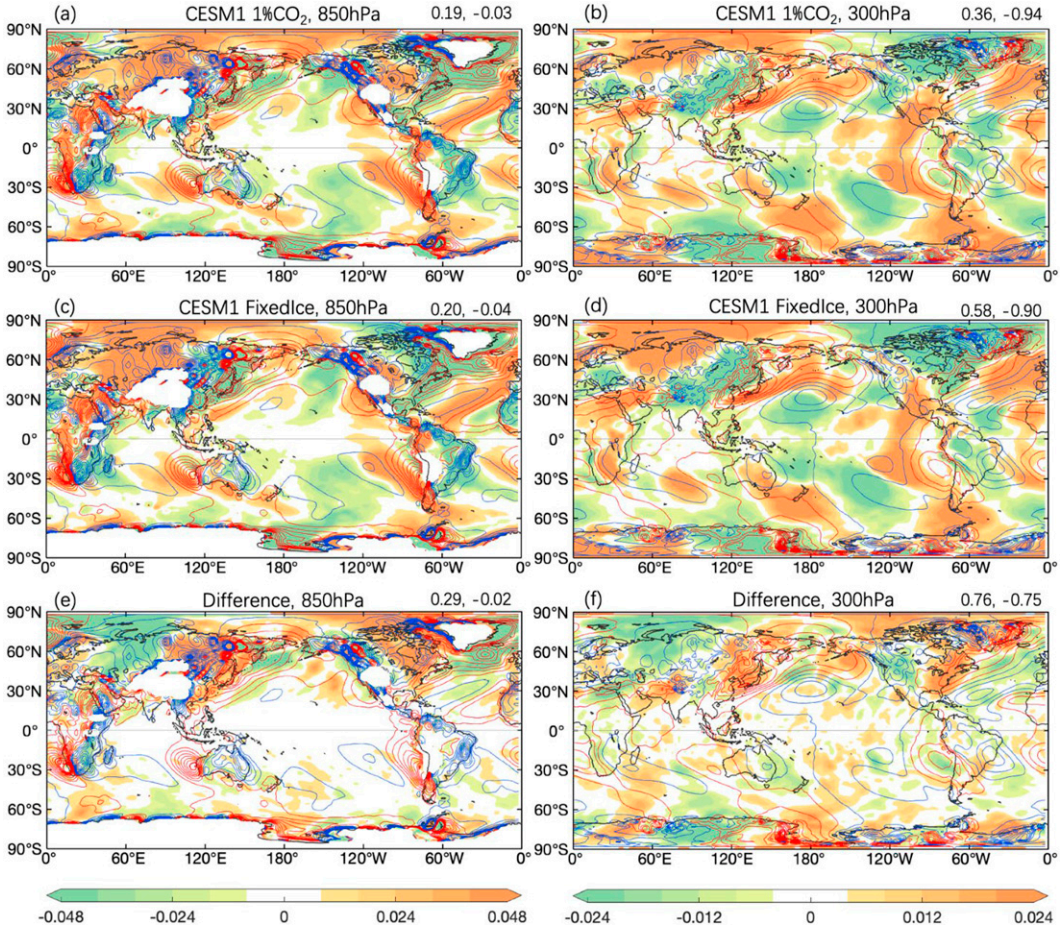

FIG. 13. CESM1-simulated October–March mean changes (relative to CTL climatology) in zonal gradients of air temperature ($\partial T/\partial x$) at (left) 850 hPa and (right) 300 hPa (shading; K per 100 km) averaged over the 20 years around the time of $4 \times CO_2$ (years 131–150) from the (a),(b) 1%CO_2 and (c),(d) FixedIce runs, and (e),(f) the 1%CO_2 minus FixedIce difference. Also shown is the CTL climatology of the zonal temperature gradients (contours, interval is 0.08 and 0.04 K per 100 km for 850 and 300 hPa, respectively, with red lines for positive and blue lines for negative values, zero contours are omitted). The pattern correlations between changes in $\partial T/\partial x$ and v over 30°–60°N and 30°–60°S are shown at the top-right corner.

the ocean feedback response (Zappa et al. 2020). Such a warming pattern should weaken the current winter cold land–warm ocean pattern, leading to weaker zonal thermal contrasts over many regions in the Northern Hemisphere (Figs. 13a–d), although the v change patterns are only weakly correlated with those of the $\partial T/\partial x$ change patterns on the same pressure level. This is due to the fact that the zonal geopotential height gradient and the geostrophic v wind should be proportional to the vertically integrated $\partial T/\partial x$, not the $\partial T/\partial x$ at the same pressure level. The zonal-mean surface and lower tropospheric warming over northern mid-to-high latitudes is much larger in the 1%CO_2 run than in FixedIce due to oceanic heating associated with sea ice loss (Dai et al. 2019; Dai and Song 2020); however, the zonal warming anomalies are stronger only over areas with large sea ice loss (e.g., the Barents–Kara Seas, Okhotsk Sea, Bering Sea, Baffin Bay, and Labrador Sea) but are weaker over most Eurasia and eastern Canada (Fig. 12e). The enhanced warming over ice-melting regions in response to Arctic sea ice loss has also been found in previous coupled model simulations (e.g., Deser et al. 2016; Smith et al. 2017). Thus, Arctic sea ice loss generally leads to a larger land–ocean temperature gradient in the northern mid-to-high latitudes (Figs. 12e,f), a pattern that is roughly opposite to the warm land–cold ocean pattern caused by the effect of CO_2 forcing without AA (Figs. 12c,d). Therefore, the effect of increased CO_2 without AA weakens the winter cold land–warm ocean pattern but the AA and Arctic sea ice loss enhances this pattern.

Besides the above-mentioned surface property differences between land and ocean, stronger westerlies under increased CO_2 can cause nonuniform warming by pushing warm ocean air into the cold land in winter and more cold land air into the ocean, leading to higher (lower) temperatures over the western side of the continents (oceans) (Molteni et al. 2011), which is not shown in Figs. 12a and 12c. Thus, the enhanced warming over land areas is unlikely to be a result of the accelerations in zonal westerlies.

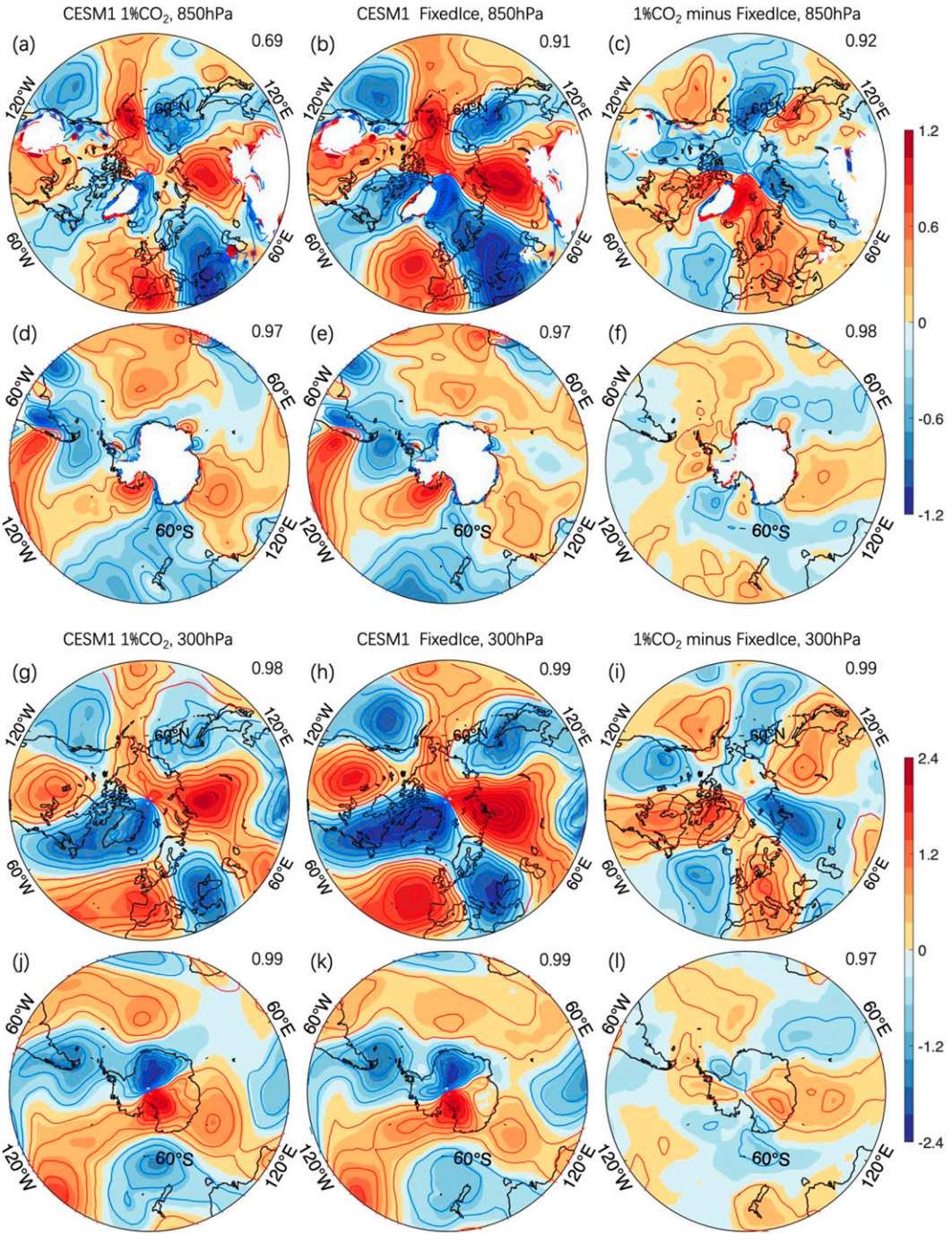

FIG. 14. October–March mean changes in geostrophic wind v_g (shading; m s^{-1}) estimated using Eq. (1) compared with the CESM1-simulated v change [contours; interval = 0.2 m s^{-1} for (a)–(f) and 0.4 m s^{-1} for (g)–(l), red for positive and blue for negative values; zero contour omitted] over (a)–(c),(g)–(i) 30°–90°N and (d)–(f),(j)–(l) 30°–90°S at 850- and 300-hPa levels averaged the 20 years (years 131–150) around of 4 × CO_2 from the (left) 1%CO_2 and (middle) FixedIce runs, and (right) the 1%CO_2 minus FixedIce difference. The pattern correlation between the shading and contours is given at the top right of each plot.

As mentioned above, the larger warming over land than over ocean (Figs. 12a–d) results mainly from different land and ocean surface properties; for example, more evaporative cooling, vertical mixing, and larger heat capacity over the oceans can reduce CO_2-induced warming. Although in theory the v changes can cause different temperature changes over different longitudes (e.g., a southerly v can lead to warm temperatures), the fact that the v change patterns (Fig. 1) do not

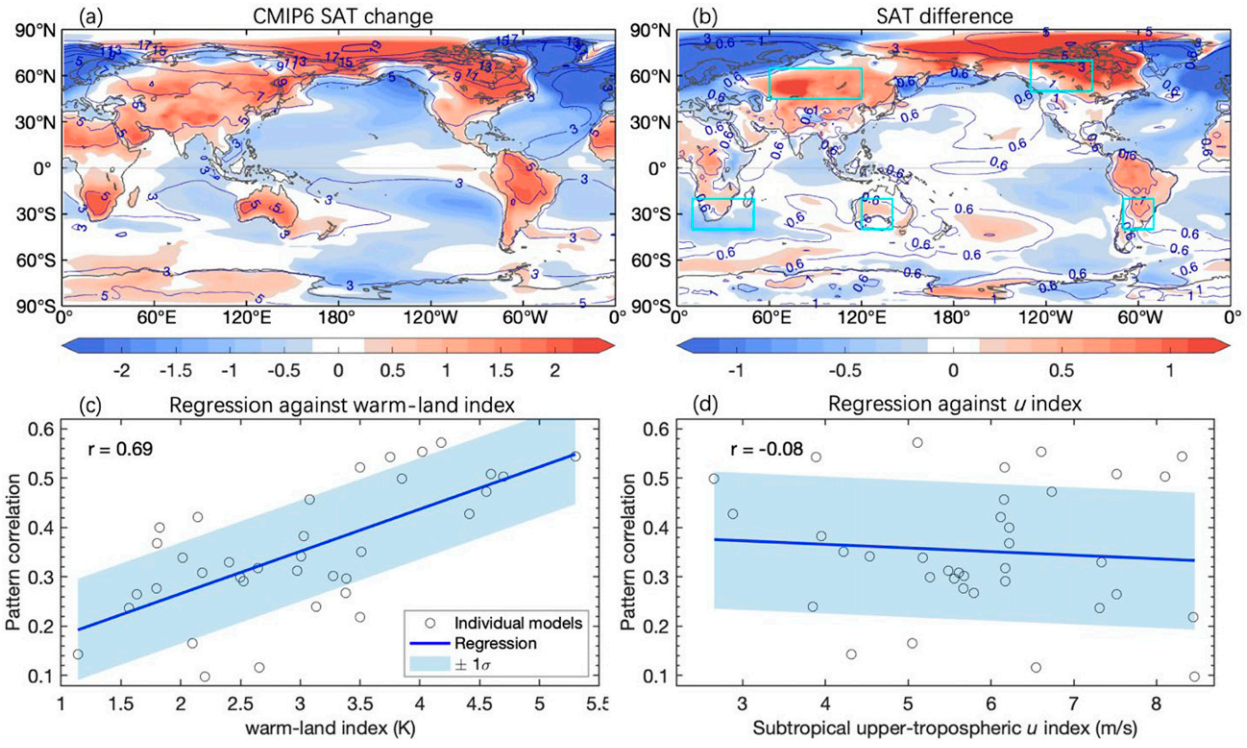

FIG. 15. (a) CMIP6 multimodel-mean SAT changes (contours; K) and their zonal anomalies (shading; deviations from the zonal mean change) averaged over October–March from 1970–99 to 2070–99 from the all-forcing historical (for 1970–2014) and SSP5–8.5 (for 2015–99) simulations averaged over the 36 CMIP6 models. (b) The differences of the SAT changes (contours; K) and their zonal anomalies (shading; deviations from the zonal mean) between the 10 CMIP6 models with V850 change pattern most similar to the CESM1-simulated V850 change pattern in the 1%CO_2 run (shown in Fig. 1a) and the other 26 CMIP6 models. Regressions of the pattern correlations between the V850 patterns in CESM1 1% CO_2 run and individual CMIP6 models against the (c) warm-land index and (d) subtropical upper-tropospheric u index calculated from individual CMIP6 models (each circle is for one model), with correlation coefficients (r) given at the top-left corner. The blue shading denotes the ±1 standard deviation range of the pattern correlations. The warm-land index is defined as the SAT zonal anomalies averaged over the regions highlighted by the cyan boxes in (b) that include northern Asia, northern North America, southern Africa, southern Australia, and southern South America. The subtropical upper-tropospheric u index is defined as the u changes at 100 hPa averaged over 20°–40°N following Simpson et al. (2016).

match the temperature change patterns (Figs. 12a–d) suggests that the impact of the v changes on the warming patterns is likely small.

Locally enhanced warming leads to positive (negative) $\partial T/\partial x$ changes on the west (east) side of the enhanced warming centers (Fig. 13). Figure 14 depicts the changes in geostrophic meridional wind v_g estimated using Eq. (1), which is governed by the changes in zonal gradient of layer-mean temperature ($\partial\overline{T}/\partial x$). It is found that the v_g changes closely match the CESM1-simulated v change (contours in Fig. 14) in terms of spatial pattern and magnitude, with strong and positive pattern correlations over 90°–30°S and 30°–90°N (shown at the top right of the panels in Fig. 14). There are regional differences near plateaus and mountains in the lower troposphere, possibly due to the friction and the errors in estimating $\overline{T}$ changes from the monthly data. The results suggest that zonally uneven warming contributes to zonally nonuniform changes in vertical thickness and geopotential height at aloft pressure levels, which can affect extratropical v via the geostrophic balance.

As shown in Fig. 15a, the CMIP6 multimodel mean SAT changes from 1970–99 to 2070–99 and the zonal anomalies are similar to the SAT changes in CESM1 1%CO_2 run shown in Fig. 12a. To examine whether the different responses in land–ocean thermal contrast among the CMIP6 models contribute to their different v responses, we chose 10 CMIP6 models with the V850 change patterns most similar to those in the 1%CO_2 runs (measured by the global pattern correlation of the V850 changes). These 10 models show a more robust WN4 (WN3) structure of the v change in the northern (southern) midlatitudes (not shown), and they tend to exhibit more enhanced warming over land than the other models (Fig. 15b). The SAT zonal anomalies averaged over the land areas highlighted by the cyan boxes in Fig. 15b are used to construct a warm-land index. Figure 15c shows that the warm-land index is strongly related to the pattern correlations of the V850 changes between the CESM1 1%CO_2 run and individual CMIP6 models. Models with a larger warm-land index exhibit a V850 change pattern more similar to that in the CESM1 1%CO_2 run with a WN4 (WN3) structure in the northern (southern) extratropics.

The warm-land index can explain almost half (~48%) of the intermodel variance in this correlation, indicating that the land warming amount has a large impact on the v response pattern in the CMIP6 models. In contrast, the intermodel spread of the pattern correlation is unrelated to subtropical upper-tropospheric u changes (Fig. 15d), which play a crucial role in the subtropical upper-tropospheric v changes (Simpson et al. 2016). The results are not very sensitive to the choice of midlatitude land areas in calculating the warm-land index; most of the sensitivity results from western Europe, where the warming response is much milder than in other continental areas at the same latitudes, likely due to the influence of the North Atlantic (Fig. 15a). Also, rescaling the changes in v, u, and warm-land index by the simulated amount of global warming in individual models did not affect the results. These results suggest that the projected v change patterns in the extratropics are linked to the model-dependent response in land–ocean thermal contrast.

The SAT change patterns in the PAMIP OAGCM models (not shown) resemble the CESM1-simulated 1%CO_2 minus FixedIce SAT difference shown in Fig. 12e, resulting in negative values of the warm-land index. The warm-land index calculated from CESM1 and HadGEM3-GC31-MM, whose v change patterns are more similar to the 1%CO_2 minus FixedIce v difference map (Figs. 6c–f), is especially negative. The PAMIP AGCM models exhibit weaker warming over the northern midlatitude oceans than the PAMIP OAGCM experiments (Peings et al. 2021). The results suggest that the v response pattern to Arctic sea ice loss is likely related to the enhanced land–ocean thermal contrast in winter; however, models may respond differently to the same amount of sea ice loss, resulting in uncertainties in the v response pattern.

5. Conclusions and discussion

In this study, we examined tropospheric v changes over the globe in response to a 4 × CO_2 increase with and without the effect of AA in CESM1, the CMIP6 model-projected v changes by the end of the twenty-first century, and the PAMIP model-simulated v response to Arctic sea ice loss. The extratropical v change pattern is approximately barotropic (i.e., with the same sign) and stronger in the boreal cold season. We found that the total v change pattern is dominated by the effect of increased CO_2 without AA. In the Northern Hemisphere, extratropical v response to increased CO_2 alone is characterized by a zonal wavenumber-4 (WN4) pattern. Arctic sea ice loss and the associated AA have an effect opposite to that of increased CO_2, generally weakening the climatological v pattern slightly. One exception is around North America where the v climatology is strengthened slightly by the effect of AA but weakened by the CO_2 forcing. The effect of AA is reduced in atmospheric model-only simulations with specified SSTs due to the strong dampening effect from fixed SSTs. Overall, the impact on current v climatology is quite small, and the zonal variance of the v climatology would increase only by ~10% over 30°–60°N due to the 4 × CO_2 forcing. However, the v changes are closely related to the meridional moisture advection and thus have significant impacts on local hydroclimates over regions like Europe. A shift to the east (by ~5° longitude) and an amplitude increase (by ~1 m s^{-1}) in the v climatology caused by the effect of increased CO_2 without AA dominates the total v change over Europe, resulting in stronger northerlies in this region and drier conditions in southern Europe, which may have contributed to the increasing droughts around the Mediterranean region (Dai 2013; Seager et al. 2019). As the changes in extratropical v significantly affect heat and moisture transport, it will be interesting to examine their contributions to the regional climate changes in the future, such as droughts in Europe (e.g., Lehner et al. 2017; Tuel and Eltahir 2020), increased precipitation in western North America (Hagos et al. 2016), and frequent droughts and wildfires in the Amazon (Duffy et al. 2015).

In the tropics, where the v climatology is weak, the v changes due to increased CO_2 alone have opposite signs in the lower and upper troposphere, closely connected to the changes in tropical convection and vertical motion. In the extratropical Southern Hemisphere, increased CO_2 generates a zonal wavenumber-3 v change pattern, which generally enhances the climatological v pattern. The effect of AA on tropospheric v wind is negligible in the tropics and Southern Hemisphere.

The CESM1-simulated v changes can be partially explained by the different warming rates over land and ocean under increasing CO_2. The effect of CO_2 forcing generally weakens the land–sea thermal contrast, while the Arctic sea ice loss tends to enhance it in the latitudes north of ~30°N. The extratropical v changes show large intermodel differences among CMIP6 models that are also linked to their different warming rates over land areas.

Change in the daily v variance is not examined here but is in Dai and Deng (2021). They showed that the increased CO_2 reduces daily v variance over most of the northern mid-to-high latitudes except central-eastern Asia, while AA has little effect on it. This result is consistent with previous findings that AA does not significantly alter waviness on synoptic or intraseasonal time scales (Hassanzadeh et al. 2014; Blackport and Screen 2020; Tierney et al. 2021). The change patterns of daily v variance in response to increased CO_2 and AA differ from those of time-mean v shown in this study (Dai and Deng 2021), suggesting that the high-frequency wave responses may reinforce or cancel themselves when averaged over time, depending on geographical locations. To understand the impact of GHG forcing and AA on extreme weather, we plan to examine the prevalence of phase and persistence of regional daily v changes in the CESM1 simulations.

Our results show that increased CO_2 and AA can change the extratropical v pattern by altering the land–ocean thermal contrasts, while the tropical v changes are related to changes in tropical convection and vertical motion. In fact, tropical convection changes can also affect the extratropical v pattern by meridionally propagating wave trains (Haarsma and Selten 2012). In addition, while the orography is fixed, adiabatic heating on orographic slopes may change in response to changes in humidity and background flow under global warming, potentially affecting the v pattern (Wills and Schneider 2018). Considering that local impacts of the v change can be significant, such as the strengthening of climatological northerlies over Europe that may exacerbate the drying in the Mediterranean region, more research is

required on the mechanisms causing regional v changes. In addition to increased CO_2 and AA, many other factors can affect land–ocean thermal contrasts. For example, increasing anthropogenic aerosols generally weaken the winter land–ocean thermal contrast outside the Arctic and have a nonlinear effect with increasing CO_2 over the northern midlatitudes (Deng et al. 2020). The impacts of external forcing besides CO_2 (e.g., anthropogenic aerosols) on the global ocean–land contrast and thus v pattern also need to be examined in future studies, although the similarity between our CESM1 and CMIP6 results suggests that the non-CO_2 forcing may play only a small role for the v change in the twenty-first century.

Acknowledgments. X. Chen was supported by the China Postdoctoral Science Foundation (BX20200087) and National Natural Science Foundation of China (42105017). A. Dai was supported by the National Science Foundation (Awards AGS-2015780 and OISE-1743738).

Data availability statement. CMIP6 and PAMIP simulations used in this study are obtained from the Earth System Grid Federation (ESGF). The CESM1 data used in this study are available from the authors upon request.

REFERENCES

Alexander, M. A., U. S. Bhatt, J. E. Walsh, M. S. Timlin, J. S. Miller, and J. D. Scott, 2004: The atmospheric response to realistic Arctic sea ice anomalies in an AGCM during winter. *J. Climate*, **17**, 890–905, https://doi.org/10.1175/1520-0442(2004)017<0890:TARTRA>2.0.CO;2.

Barnes, E. A., 2013: Revisiting the evidence linking Arctic amplification to extreme weather in midlatitudes. *Geophys. Res. Lett.*, **40**, 4728–4733, https://doi.org/10.1002/grl.50880.

Blackport, R., and P. J. Kushner, 2017: Isolating the atmospheric circulation response to Arctic sea ice loss in the coupled climate system. *J. Climate*, **30**, 2163–2185, https://doi.org/10.1175/JCLI-D-16-0257.1.

——, and J. A. Screen, 2020: Insignificant effect of Arctic amplification on the amplitude of midlatitude atmospheric waves. *Sci. Adv.*, **6**, eaay2880, https://doi.org/10.1126/sciadv.aay2880.

Chen, J., A. Dai, and Y. Zhang, 2019: Projected changes in daily variability and seasonal cycle of near-surface air temperature over the globe during the twenty-first century. *J. Climate*, **32**, 8537–8561, https://doi.org/10.1175/JCLI-D-19-0438.1.

Chen, X., D. Luo, Y. Wu, E. Dunn-Sigouin, and J. Lu, 2021: Nonlinear response of atmospheric blocking to early winter Barents–Kara Seas warming: An idealized model study. *J. Climate*, **34**, 2367–2383, https://doi.org/10.1175/JCLI-D-19-0720.1.

Cohen, J., L. Agel, M. Barlow, C. I. Garfinkel, and I. White, 2021: Linking Arctic variability and change with extreme winter weather in the United States. *Science*, **373**, 1116–1121, https://doi.org/10.1126/science.abi9167.

Dai, A., 2013: Increasing drought under global warming in observations and models. *Nat. Climate Change*, **3**, 52–58, https://doi.org/10.1038/nclimate1633.

——, and M. Song, 2020: Little influence of Arctic amplification on mid-latitude climate. *Nat. Climate Change*, **10**, 231–237, https://doi.org/10.1038/s41558-020-0694-3.

——, and J. Deng, 2021: Arctic amplification weakens the variability of daily temperatures over northern middle-high latitudes. *J. Climate*, **34**, 2591–2609, https://doi.org/10.1175/JCLI-D-20-0514.1.

——, A. Hu, G. A. Meehl, W. M. Washington, and W. G. Strand, 2005: Atlantic thermohaline circulation in a coupled general circulation model: Unforced variations versus forced changes. *J. Climate*, **18**, 3270–3293, https://doi.org/10.1175/JCLI3481.1.

——, H. Li, Y. Sun, L.-C. Hong, Linho, C. Chou, and T. Zhou, 2013: The relative roles of upper and lower tropospheric thermal contrasts and tropical influences in driving Asian summer monsoons. *J. Geophys. Res. Atmos.*, **118**, 7024–7045, https://doi.org/10.1002/jgrd.50565.

——, D. Luo, M. Song, and J. Liu, 2019: Arctic amplification is caused by sea-ice loss under increasing CO_2. *Nat. Commun.*, **10**, 121, https://doi.org/10.1038/s41467-018-07954-9.

Davis, N., and T. Birner, 2017: On the discrepancies in tropical belt expansion between reanalyses and climate models and among tropical belt width metrics. *J. Climate*, **30**, 1211–1231, https://doi.org/10.1175/JCLI-D-16-0371.1.

Deng, J., A. Dai, and H. Xu, 2020: Nonlinear climate responses to increasing CO_2 and anthropogenic aerosols simulated by CESM. *J. Climate*, **33**, 281–301, https://doi.org/10.1175/JCLI-D-19-0195.1.

Deser, C., R. A. Tomas, M. Alexander, and D. Lawrence, 2010: The seasonal atmospheric response to projected Arctic sea ice loss in the late twenty-first century. *J. Climate*, **23**, 333–351, https://doi.org/10.1175/2009JCLI3053.1.

——, ——, and L. Sun, 2015: The role of ocean–atmosphere coupling in the zonal-mean atmospheric response to Arctic sea ice loss. *J. Climate*, **28**, 2168–2186, https://doi.org/10.1175/JCLI-D-14-00325.1.

——, L. Sun, R. A. Tomas, and J. Screen, 2016: Does ocean coupling matter for the northern extratropical response to projected Arctic sea ice loss? *Geophys. Res. Lett.*, **43**, 2149–2157, https://doi.org/10.1002/2016GL067792.

Duffy, P. B., P. Brando, G. P. Asner, and C. B. Field, 2015: Projections of future meteorological drought and wet periods in the Amazon. *Proc. Natl. Acad. Sci. USA*, **112**, 13 172–13 177, https://doi.org/10.1073/pnas.1421010112.

England, M. R., L. M. Polvani, L. Sun, and C. Deser, 2020: Tropical climate responses to projected Arctic and Antarctic sea-ice loss. *Nat. Geosci.*, **13**, 275–281, https://doi.org/10.1038/s41561-020-0546-9.

Eyring, V., S. Bony, G. A. Meehl, C. A. Senior, B. Stevens, R. J. Stouffer, and K. E. Taylor, 2016: Overview of the Coupled Model Intercomparison Project Phase 6 (CMIP6) experimental design and organization. *Geosci. Model Dev.*, **9**, 1937–1958, https://doi.org/10.5194/gmd-9-1937-2016.

Francis, J. A., and S. J. Vavrus, 2012: Evidence linking Arctic amplification to extreme weather in mid-latitudes. *Geophys. Res. Lett.*, **39**, L06801, https://doi.org/10.1029/2012GL051000.

——, and ——, 2015: Evidence for a wavier jet stream in response to rapid Arctic warming. *Environ. Res. Lett.*, **10**, 014005, https://doi.org/10.1088/1748-9326/10/1/014005.

Geng, Y.-F., S.-P. Xie, X.-T. Zheng, and C.-Y. Wang, 2020: Seasonal dependency of tropical precipitation change under global warming. *J. Climate*, **33**, 7897–7908, https://doi.org/10.1175/JCLI-D-20-0032.1.

Haarsma, R. J., and F. Selten, 2012: Anthropogenic changes in the Walker circulation and their impact on the extra-tropical planetary wave structure in the Northern Hemisphere.

Climate Dyn., **39**, 1781–1799, https://doi.org/10.1007/s00382-012-1308-1.

Hagos, S. M., L. R. Leung, J.-H. Yoon, J. Lu, and Y. Gao, 2016: A projection of changes in landfalling atmospheric river frequency and extreme precipitation over western North America from the large ensemble CESM simulations. *Geophys. Res. Lett.*, **43**, 1357–1363, https://doi.org/10.1002/2015GL067392.

Hassanzadeh, P., Z. Kuang, and B. F. Farrell, 2014: Responses of midlatitude blocks and wave amplitude to changes in the meridional temperature gradient in an idealized dry GCM. *Geophys. Res. Lett.*, **41**, 5223–5232, https://doi.org/10.1002/2014GL060764.

Hersbach, H., and Coauthors, 2020: The ERA5 global reanalysis. *Quart. J. Roy. Meteor. Soc.*, **146**, 1999–2049, https://doi.org/10.1002/qj.3803.

Hitchcock, P., and I. R. Simpson, 2014: The downward influence of stratospheric sudden warmings. *J. Atmos. Sci.*, **71**, 3856–3876, https://doi.org/10.1175/JAS-D-14-0012.1.

Holton, J. R., 2004: *An Introduction to Dynamic Meteorology*. R. Dmowska, J. R. Holton, and H. T. Rossby, Eds., Elsevier, 535 pp.

Hurrell, J. W., and Coauthors, 2013: The Community Earth System Model: A framework for collaborative research. *Bull. Amer. Meteor. Soc.*, **94**, 1339–1360, https://doi.org/10.1175/BAMS-D-12-00121.1.

Jenkins, M. T. and A. Dai, 2021: The impact of sea-ice loss on Arctic climate feedbacks and their role for Arctic amplification. *Geophys. Res. Lett.*, **48**, e2021GL094599, https://doi.org/10.1029/2021GL094599.

Joshi, M. M., F. H. Lambert, and M. J. Webb, 2013: An explanation for the difference between twentieth and twenty-first century land–sea warming ratio in climate models. *Climate Dyn.*, **41**, 1853–1869, https://doi.org/10.1007/s00382-013-1664-5.

Kim, B.-M., S.-W. Son, S.-K. Min, J.-H. Jeong, S.-J. Kim, X. Zhang, S. Taehyoun, and J.-H. Yoon, 2014: Weakening of the stratospheric polar vortex by Arctic sea-ice loss. *Nat. Commun.*, **5**, 4646, https://doi.org/10.1038/ncomms5646.

Lee, J. Y., and Coauthors, 2021: Future global climate: Scenario-based projections and near-term information. *Climate Change 2021: The Physical Science Basis*. V. Masson-Delmotte et al., Eds., Cambridge University Press, 553–672.

Lee, S. L., P. D. Williams, and T. H. A. Frame, 2019: Increased shear in the North Atlantic upper-level jet stream over the past four decades. *Nature*, **572**, 639–642, https://doi.org/10.1038/s41586-019-1465-z.

Lehner, F., S. Coats, T. F. Stocker, A. G. Pendergrass, B. M. Sanderson, C. C. Raible, and J. E. Smerdon, 2017: Projected drought risk in 1.5°C and 2°C warmer climates. *Geophys. Res. Lett.*, **44**, 7419–7428, https://doi.org/10.1002/2017GL074117.

Liu, J., J. A. Curry, H. Wang, M. Song, and R. M. Horton, 2012: Impact of declining Arctic sea ice on winter snowfall. *Proc. Natl. Acad. Sci. USA*, **109**, 4074–4079, https://doi.org/10.1073/pnas.1114910109.

Lu, J., G. Chen, and D. M. W. Frierson, 2008: Response of the zonal mean atmospheric circulation to El Niño versus global warming. *J. Climate*, **21**, 5835–5851, https://doi.org/10.1175/2008JCLI2200.1.

Luo, B., L. Wu, D. Luo, A. Dai, and I. Simmonds, 2019: The winter midlatitude-Arctic interaction: Effects of North Atlantic SST and high-latitude blocking on Arctic sea ice and Eurasian cooling. *Climate Dyn.*, **52**, 2981–3004, https://doi.org/10.1007/s00382-018-4301-5.

Luo, D., Y. Xiao, Y. Yao, A. Dai, I. Simmonds, and C. L. E. Franzke, 2016: Impact of Ural blocking on winter warm Arctic–cold Eurasian anomalies. Part I: Blocking-induced amplification. *J. Climate*, **29**, 3925–3947, https://doi.org/10.1175/JCLI-D-15-0611.1.

——, X. Chen, A. Dai, and I. Simmonds, 2018: Changes in atmospheric blocking circulations linked with winter Arctic warming: A new perspective. *J. Climate*, **31**, 7661–7678, https://doi.org/10.1175/JCLI-D-18-0040.1.

Mamalakis, A., and Coauthors, 2021: Zonally contrasting shifts of the tropical rain belt in response to climate change. *Nat. Climate Change*, **11**, 143–151, https://doi.org/10.1038/s41558-020-00963-x.

Manabe, S., R. J. Stouffer, M. J. Spelman, and K. Bryan, 1991: Transient responses of a coupled ocean–atmosphere model to gradual changes of atmospheric CO_2. Part I. Annual mean response. *J. Climate*, **4**, 785–818, https://doi.org/10.1175/1520-0442(1991)004<0785:TROACO>2.0.CO;2.

Manney, G. L., and M. I. Hegglin, 2018: Seasonal and regional variations of long-term changes in upper-tropospheric jets from reanalyses. *J. Climate*, **31**, 423–448, https://doi.org/10.1175/JCLI-D-17-0303.1.

Marshall, J., J. R. Scott, K. C. Armour, J.-M. Campin, M. Kelley, and A. Romanou, 2015: The ocean's role in the transient response of climate to abrupt greenhouse gas forcing. *Climate Dyn.*, **44**, 2287–2299, https://doi.org/10.1007/s00382-014-2308-0.

McCusker, K. E., P. J. Kushner, J. C. Fyfe, M. Sigmond, V. V. Kharin, and C. M. Bitz, 2017: Remarkable separability of circulation response to Arctic sea ice loss and greenhouse gas forcing. *Geophys. Res. Lett.*, **44**, 7955–7964, https://doi.org/10.1002/2017GL074327.

Miao, J., T. Wang, and D. Chen, 2020: More robust changes in the East Asian winter monsoon from 1.5° to 2.0°C global warming targets. *Int. J. Climatol.*, **40**, 4731–4749, https://doi.org/10.1002/joc.6485.

Molteni, F., M. P. King, F. Kucharski, and D. M. Straus, 2011: Planetary-scale variability in the northern winter and the impact of land–sea thermal contrast. *Climate Dyn.*, **37**, 151–170, https://doi.org/10.1007/s00382-010-0906-z.

Mori, M., M. Watanabe, H. Shiogama, J. Inoue, and M. Kimoto, 2014: Robust Arctic sea-ice influence on the frequent Eurasian cold winters in past decades. *Nat. Geosci.*, **7**, 869–873, https://doi.org/10.1038/ngeo2277.

Nakamura, T., K. Yamazaki, K. Iwamoto, M. Honda, Y. Miyoshi, Y. Ogawa, Y. Tomikawa, and J. Ukita, 2016: The stratospheric pathway for Arctic impacts on midlatitude climate. *Geophys. Res. Lett.*, **43**, 3494–3501, https://doi.org/10.1002/2016GL068330.

O'Neill, B. C., and Coauthors, 2016: The Scenario Model Intercomparison Project (ScenarioMIP) for CMIP6. *Geosci. Model Dev.*, **9**, 3461–3482, https://doi.org/10.5194/gmd-9-3461-2016.

Peings, Y., J. Cattiaux, and H. Douville, 2013: Evaluation and response of winter cold spells over western Europe in CMIP5 models. *Climate Dyn.*, **41**, 3025–3037, https://doi.org/10.1007/s00382-012-1565-z.

——, Z. M. Labe, and G. Magnusdottir, 2021: Are 100 ensemble members enough to capture the remote atmospheric response to +2°C Arctic sea ice loss? *J. Climate*, **34**, 3751–3769, https://doi.org/10.1175/JCLI-D-20-0613.1.

Rayner, N. A., D. E. Parker, E. B. Horton, C. K. Folland, L. V. Alexander, D. P. Rowell, E. C. Kent, and A. Kaplan, 2003: Global analyses of sea surface temperature, sea ice, and night marine air temperature since the late nineteenth century. *J. Geophys. Res.*, **108**, 4407, https://doi.org/10.1029/2002JD002670.

Seager, R., T. J. Osborn, Y. Kushnir, I. R. Simpson, J. Nakamura, and H. Liu, 2019: Climate variability and change of Mediterranean-type climates. *J. Climate*, **32**, 2887–2915, https://doi.org/10.1175/JCLI-D-18-0472.1.

Serreze, M. C., and J. A. Francis, 2006: The Arctic amplification debate. *Climatic Change*, **76**, 241–264, https://doi.org/10.1007/s10584-005-9017-y.

Shoji, T., Y. Kanno, T. Iwasaki, and K. Takaya, 2014: An isentropic analysis of the temporal evolution of East Asian cold air outbreaks. *J. Climate*, **27**, 9337–9348, https://doi.org/10.1175/JCLI-D-14-00307.1.

Simpson, I. R., R. Seager, M. Ting, and T. A. Shaw, 2016: Causes of change in Northern Hemisphere winter meridional winds and regional hydroclimate. *Nat. Climate Change*, **6**, 65–70, https://doi.org/10.1038/nclimate2783.

Smith, D. M., N. J. Dunstone, A. A. Scaife, E. K. Fiedler, D. Copsey, and S. C. Hardiman, 2017: Atmospheric response to Arctic and Antarctic sea ice: The importance of ocean–atmosphere coupling and the background state. *J. Climate*, **30**, 4547–4565, https://doi.org/10.1175/JCLI-D-16-0564.1.

——, and Coauthors, 2019: The Polar Amplification Model Intercomparison Project (PAMIP) contribution to CMIP6: Investigating the causes and consequences of polar amplification. *Geosci. Model Dev.*, **12**, 1139–1164, https://doi.org/10.5194/gmd-12-1139-2019.

Sun, L., C. Deser, and R. A. Tomas, 2015: Mechanisms of stratospheric and tropospheric circulation response to projected Arctic sea ice loss. *J. Climate*, **28**, 7824–7845, https://doi.org/10.1175/JCLI-D-15-0169.1.

——, M. Alexander, and C. Deser, 2018: Evolution of the global coupled climate response to Arctic sea ice loss during 1990–2090 and its contribution to climate change. *J. Climate*, **31**, 7823–7843, https://doi.org/10.1175/JCLI-D-18-0134.1.

Sussman, H. S., A. Raghavendra, P. E. Roundy, and A. Dai, 2020: Trends in northern midlatitude atmospheric wave power from 1950 to 2099. *Climate Dyn.*, **54**, 2903–2918, https://doi.org/10.1007/s00382-020-05143-3.

Tierney, G., W. A. Robinson, G. Lackmann, and R. Miller, 2021: The sensitivity of persistent geopotential anomalies to the climate of a moist channel model. *J. Climate*, **34**, 5093–5108, https://doi.org/10.1175/JCLI-D-20-0254.1.

Tuel, A., and E. A. B. Eltahir, 2020: Why is the Mediterranean a climate change hot spot? *J. Climate*, **33**, 5829–5843, https://doi.org/10.1175/JCLI-D-19-0910.1.

——, P. A. O'Gorman, and E. A. B. Eltahir, 2021: Elements of the dynamical response to climate change over the Mediterranean. *J. Climate*, **34**, 1135–1146, https://doi.org/10.1175/JCLI-D-20-0429.1.

Wang, L., and W. Chen, 2014: The East Asian winter monsoon: Re-amplification in the mid-2000s. *Chin. Sci. Bull.*, **59**, 430–436, https://doi.org/10.1007/s11434-013-0029-0.

Wills, R. C. J., and T. Schneider, 2018: Mechanisms setting the strength of orographic Rossby waves across a wide range of climates in a moist idealized GCM. *J. Climate*, **31**, 7679–7700, https://doi.org/10.1175/JCLI-D-17-0700.1.

——, R. H. White, and X. J. Levine, 2019: Northern Hemisphere stationary waves in a changing climate. *Curr. Climate Change Rep.*, **5**, 372–389, https://doi.org/10.1007/s40641-019-00147-6.

Xue, D., J. Lu, L. Sun, G. Chen, and Y. Zhang, 2017: Local increase of anticyclonic wave activity over northern Eurasia under amplified Arctic warming. *Geophys. Res. Lett.*, **44**, 3299–3308, https://doi.org/10.1002/2017GL072649.

Yao, Y., D. Luo, A. Dai, and I. Simmonds, 2017: Increased quasi-stationarity and persistence of Ural blocking and Eurasian extreme cold events in response to Arctic warming. Part I: Insights from observational analyses. *J. Climate*, **30**, 3549–3568, https://doi.org/10.1175/JCLI-D-16-0261.1.

Zappa, G., P. Ceppi, and T. G. Shepherd, 2020: Time-evolving sea-surface warming patterns modulate the climate change response of subtropical precipitation over land. *Proc. Natl. Acad. Sci. USA*, **117**, 4539–4545, https://doi.org/10.1073/pnas.1911015117.

Zhang, P., Y. Wu, I. R. Simpson, K. Smith, X. Zhang, B. De, and P. Callaghan, 2018: A stratospheric pathway linking a colder Siberia to Barents-Kara Sea sea ice loss. *Sci. Adv.*, **4**, eaat6025, https://doi.org/10.1126/sciadv.aat6025.